國立臺灣大學電機資訊學院電信工程學研究所

碩士論文

Graduate Institute of Communication Engineering
College of Electrical Engineering and Computer Science
National Taiwan University

Master's Thesis

基於裝載二極體之一位元可重構式寬頻穿透陣列單元及其直流偏壓走線設計

Wideband 1-Bit Reconfigurable Transmitarray Unit Cell Based on PIN Diode Loading and Its DC Bias Routing Design

林柏廷

Bo-Ting Lin

指導教授：陳士元 博士

Advisor: Shih-Yuan Chen, Ph.D.

中華民國 112 年 7 月

July 2023

doi:10.6342/NTU202302000

國立臺灣大學碩士學位論文
口試委員會審定書
MASTER'S THESIS ACCEPTANCE CERTIFICATE
NATIONAL TAIWAN UNIVERSITY

基於裝載二極體之一位元可重構式寬頻穿透陣列單元及其直流偏壓走線設計

Wideband 1-Bit Reconfigurable Transmitarray Unit Cell Based on PIN Diode Loading and Its DC Bias Routing Design

本論文係 林柏廷 (姓名) R10942018 （學號）在國立臺灣大學電信所 (系/所/學位學程)完成之碩士學位論文，於民國 112 年 7 月 18 日承下列考試委員審查通過及口試及格，特此證明。

The undersigned, appointed by the Department / Institute of Communication Engineering on 18 (date) 7 (month) 2023 (year) have examined a Master's thesis entitled above presented by Bo-Ting Lin (name) R10942018 (student ID) candidate and hereby certify that it is worthy of acceptance.

口試委員 Oral examination committee:

陳士元
（指導教授 Advisor）

系主任/所長 Director:

誌謝

首先，感謝常常在半夜用工作站跑模擬的我自己，你的努力我都有看在眼裡，也恭喜你最後的板子會動，不可控因素如此之多，能一個半月內搞定根本奇蹟。回想當初剛踏入電波領域，懵懂的我修專題時走了不少歪路，有幸能跟隨陳士元教授這盞明燈的指引，逐步培養出作為一個研究生該有的樣子。此外陳士元教授也亦師亦友，許多鼓勵以及建議都十分一語中的，我在往後的人生中都會銘記在心。再來，我要感謝我的家人們，在我無數個躲在房間裡肝苦的日子，都不曾讓我餓到，沒有你們的支持與學費，我肯定沒辦法完成這份碩士論文。另外，也感謝謝宜霈女士迄今八年來的陪伴，希望未來的日子我們依舊能互相扶持，大不了妳養我。

也非常感謝實驗室中的每一個人，感謝吳聖偉學長，雖然我常常跑籃球場，都跟不到學長的夜跑團，但在實驗室跟學長的閒聊中總能收獲滿滿；感謝許瑞福學長，不論是量測上還是各種儀器的使用上都常常給予大力協助，也算是延續了大一車車課的緣分；感謝黃慕召學長、Robin 學長以及 Louis 學長，即使較少碰面，還是能提供我寶貴的建議，幫助我確立研究方向；感謝黃士銘學長，都會熱心的跟我討論各種研究上會遇到實際問題，這我就當作是你借用我位子的補償囉！感謝詹昀穎學姊、楊欣融學長，在申請交換學生的路上幫了我很多很多；感謝蔡昀廷、毛冠勛、陳士允以及 Saurav，沒有你們，我的碩班生活不會有這麼多零食以及歡笑，跟你們一起做研究是我一輩子珍貴的回憶。

最後，我想感謝碩士論文的口試委員們：馬自莊教授、廖文照教授、陳念偉教授以及歐陽良昱教授，感謝你們在口試前後的鼓勵與稱讚，並給予許多寶貴的建議讓我能完善這份碩士論文。

doi:10.6342/NTU202302000

中文摘要

在即將到來的 B5G/6G 無線通訊中，穿透陣列天線可用於波束控制應用。本論文中，我們提出了一種寬頻、裝載二極體之穿透陣列天線單元，可應用於在穿透陣列天線上的每個位置生成一位元可切換的穿透相位補償。我們添加了多種結構來改善二極體的負載影響。其 3-dB 插入損失頻寬為 23.8%，頻寬內最小的插入損失為 0.798 dB。為了驗證模擬結果的正確性，我們採用波導量測技術對此穿透陣列天線單元進行量測，其結果與模擬一致。

此外，可重構式穿透陣列天線須有合適的直流偏壓走線設計來為每一個穿透陣列天線單元提供獨立且特定的直流偏壓。然而，直流偏壓走線將無可避免地覆蓋整個穿透陣列，進而影響其穿透性能。另一方面，一般穿透陣列天線的單元數量往往相當龐大，若使用離散元件隔離單元內的直流及射頻訊號，則所需之元件數將十分可觀，且會提高製作的困難度。在不使用其他離散元件進行直流及射頻訊號隔離之條件下，為了減少直流偏壓走線的影響，本論文針對穿透陣列天線的直流偏壓走線設計進行討論。首先，透過文獻回顧，我們總結了前人的論文並歸納出直流偏壓走線的規則。接著，吾人提出四種直流偏壓走線的設計。其中，前兩種設計乃基於基本走線規則，而後兩種設計則是基於進階走線規則。此外，為了評估不同的直流偏壓走線設計的影響，我們亦提出兩種模擬方式。

最後，為了驗證吾人所提出的穿透陣列天線單元及直流偏壓走線設計，我們實作出操作於 X 頻段的 64 單元可重構式穿透陣列天線，並在微波暗室中進行量測。然受限於製作成本，該一位元可重構式穿透陣列天線原型僅有 64 單元，故在 11.5 GHz 的增益為 9.1 dBi，3-dB 增益頻寬為 25%。所測得的波束掃描範圍及對應之損

doi:10.6342/NTU202302000

耗為 40° (2.3 dB) × 40° (3.3 dB)。此結果驗證了所提出的一位元可重構式穿透陣列天線單元及直流偏壓走線的可行性。

關鍵字: 波束掃描、直流偏壓走線設計、二極體、可重構式、穿透陣列天線

doi:10.6342/NTU202302000

ABSTRACT

In the emerging B5G/6G wireless communications, transmitarrays are promising candidates for beam-steering applications. In this work, a wideband PIN-diode-loaded transmitarray unit cell is proposed to generate 1-bit phase compensation at each location on the transmitarray. Several modifications are added to mitigate the loading effect of the PIN diodes. The 3-dB insertion loss bandwidth is 23.8%, and the minimum insertion loss is 0.798 dB. For verification, the waveguide measurement technique is adopted to characterize the proposed 1-bit reconfigurable unit cell. The measured results are consistent with those simulated.

Besides, for a reconfigurable transmitarray, proper DC bias routing design is critical to provide each unit cell with the desired DC bias voltages while not affecting its RF performance. However, the DC bias routing will inevitably cover the transmitarray surface and thus degrade the transmission performance of the transmitarray. On the other hand, the number of unit cells of a transmitarray antenna is in general relatively large. If discrete components are used to isolate the DC and RF signals in each unit cell, then an excessive number of components will be needed, increasing significantly the fabrication cost and complexity. Therefore, under the constraint of not using discrete components for DC and RF isolation, design considerations for reducing the impact imposed by DC bias routing in a reconfigurable transmitarray formed by the proposed unit cell is presented. Through the literature survey, some routing guidelines are derived from the previous works. Then, four designs of DC bias routing are proposed. Two of them are based on general routing rules, whereas the other two are based on advanced routing rules. Also, two simulation methods are introduced to evaluate the influence of different DC bias

doi:10.6342/NTU202302000

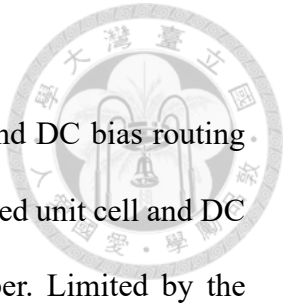

routing designs.

Lastly, to further verify the efficacy of the proposed unit cell and DC bias routing design, an 8×8 1-bit reconfigurable transmitarray based on the proposed unit cell and DC bias routing design is fabricated and tested in the anechoic chamber. Limited by the fabrication cost, such an 8×8 reconfigurable transmitarray shows only a broadside gain of 9.1 dBi at 11.5 GHz and a 3-dB gain bandwidth of 25%. The achieved beam scanning range and loss for the two principal cut planes are 40° (2.3 dB) × 40° (3.3 dB). The feasibility of the proposed 1-bit reconfigurable transmitarray unit cell and its DC routing design is verified.

Keywords: beam-steering, DC bias routing design, PIN diodes, reconfigurable, transmitarrays

doi:10.6342/NTU202302000

CONTENTS

doi:10.6342/NTU202302000

doi:10.6342/NTU202302000

doi:10.6342/NTU202302000

LIST OF FIGURES

doi:10.6342/NTU202302000

doi:10.6342/NTU202302000

doi:10.6342/NTU202302000

doi:10.6342/NTU202302000

LIST OF TABLES

doi:10.6342/NTU202302000

Chapter 1 Introduction

1.1 Background

In the upcoming B5G/6G era, satellite communication, radar system, and remote sensing are growing rapidly and used in various wireless communication scenarios. As the operating frequency gets higher and higher, severe propagation loss is one of the big challenges needed to be overcome. There are two popular solutions for this, small cell base station and beam steering. The small cell base station is aiming to adapt to the small transmission range under the 5G/B5G environment, while beam steering is to concentrate the transmission power to the desired direction by applying the phased array theory. Unlike traditional wide-beam antennas used in base stations, the beam steering capability can enhance the system throughput without wasting much energy.

To realize beam steering, an antenna array is mostly used. Transmitarray (TA) is a type of antenna array without the blockage effect of reflectarray (RA) due to its feed antenna and without the lossy and complicated feeding network of traditional antenna arrays. A typical unit cell design of TA is to separately design its receiving and transmitting antennas, forming a receive-transmit structure (Rx-Tx). Such a structure requires multiple metallic vias to transfer RF signals between the receiving and transmitting antenna elements. Consequently, a Rx-Tx-based unit cell usually requires multiple layers and vias with complex structures. Another method is based on the frequency-selective surface (FSS). The receiver and transmitter of the FSS-based unit cell are designed at the same time, and the incident wave is propagating through by coupling between multiple layers.

doi:10.6342/NTU202302000

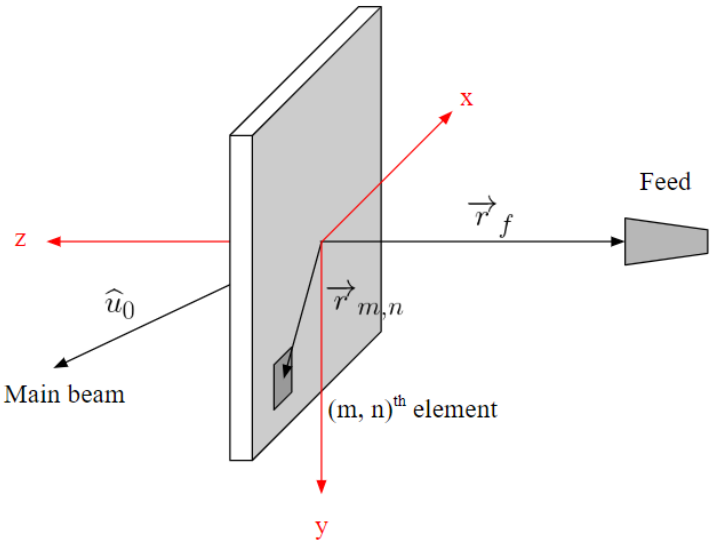

Fig. 1.1. The coordinate system of a planar TA.

By controlling the phase shift of each antenna element of an antenna array, the main beam can be pointed in a desired direction. Based on the design guideline for TA [1], as shown in Fig. 1.1, to form a main beam in the direction $\hat{u}_0$, the required phase shift $\varphi_{m,n}$ of the (m, n)th element on a planar M×N TA can be expressed as (1.1), where φ_0 is the reference phase.

$$\varphi_{m,n} = k\left(\left|\vec{r}_{m,n} - \vec{r}_f\right| - \vec{r}_{m,n} \cdot \hat{u}_0\right) + \varphi_0 \tag{1.1}$$

There are two categories to generate the required phase shift distribution, continuous phase tuning, and discrete phase switching. For continuous phase tuning, [2] adds a phase shifter between its receiver and transmitter. Although it is reconfigurable, it is also very bulky and complex due to its Rx-Tx structure. As for the FSS-based unit cells, the continuous phase shift of the unit cell is generated by tuning the geometrical parameters [3], [4]. Not only numerous parametric studies are needed, the bandwidth is quite narrow because all unit cells with different phase shifts have to overlap their operating bands. Besides, reconfigurable continuous phase tuning can be realized by mechanical rotation

doi:10.6342/NTU202302000

or using varactors to provide phase shift. However, mechanical rotation is relatively slow and varactors usually have limited phase tuning range. Therefore, the concept of discrete phase switching is getting popular nowadays, especially for the implementation of beam-steering TAs.

Discrete phase switching is also called N-bits phase quantization. For any given integer N, the continuous 360° phase range is discretized into 2^N points, as expressed in (1.2).

$$\varphi_{m,n}^{q_{N-bits}} = \begin{cases} 0°, & \text{if } \dfrac{-180°}{2^N} \le \varphi_{m,n} \le \dfrac{180°}{2^N} \\ \dfrac{1}{2^N} \cdot 360°, & \text{if } \dfrac{180°}{2^N} \le \varphi_{m,n} \le \dfrac{540°}{2^N} \\ \vdots & \\ \dfrac{2^N - 1}{2^N} \cdot 360°, & \text{other cases} \end{cases} \tag{1.2}$$

The simplest one among them is the 1-bit phase quantization, where (1.2) can be reduced to (1.3).

$$\varphi_{m,n}^{q_{1-bit}} = \begin{cases} 0°, & \text{if } -90° \le \varphi_{m,n} \le 90° \\ 180°, & \text{other cases} \end{cases} \tag{1.3}$$

It is much easier to provide either 0° or 180° phase shift by using active elements, such as varactors or PIN diodes. For the FSS-based design, active elements can be used to directly modulate the unit cell response, say using varactors to shift the resonant frequencies together [5], or using PIN diodes to change the aperture shape [6], [7]. Mostly, the bandwidths of such unit cells operating at the states of 0° and 180° phase shifts are different from each other. Thus, the resultant narrower bandwidth limits its application. Obviously, it is required that the bandwidth of both states of 1-bit RTA unit cells should be identical but only with a 180° phase difference.

In fact, the 180° phase difference can be generated by an opposite-polarized unit cell

doi:10.6342/NTU202302000

pair. If 1-bit TA unit cell pairs are designed with mirror symmetry, they will have the same operating band but opposite polarization direction, and hence 180° phase difference. For Rx-Tx-based designs, PIN diodes are added to control the polarization direction either on the mirror-symmetry receiver [8], [9], or on the mirror-symmetry transmitter [10]-[12]. However, in the FSS-based designs, metallic vias are not necessary to transfer the RF signal. To realize the same operating band with opposite polarization direction, the polarization-rotated unit cells have been studied [13]-[16]. Such designs are based on the polarization-rotating mutual coupling mechanism, that is, the polarization of the incident wave will be rotated horizontally by 90° for a 0° phase shift and by -90° for a 180° phase shift under the same mutual coupling mechanism so that an opposite-polarized unit cell pair with the same operating band can be generated. Thus, PIN diodes are added in the FSS-based design to control the orientation of the aperture for polarization-rotating mutual coupling [17]-[19].

1.2 Motivation

The aforementioned active-element-loaded unit cells can be used to form a reconfigurable transmitarray (RTA). Among them, the Rx-Tx-based designs usually have a higher design complexity and multiple layers and vias. The FSS-based designs are relatively simpler and low-profile. However, in [14]-[18], two polarizer layers and at least one air layer are used to help achieve the polarization selection for receiving and transmitting waves. On the contrary, [13] can perform polarization selection with only two substrate layers. Furthermore, there are three resonant modes existing inside its simple structure, which makes it a wideband unit cell. Therefore, we take advantage of the low profile and wideband feature of [13] and modify it to become reconfigurable,

doi:10.6342/NTU202302000

which we proposed previously in [20] and further improved in this thesis.

On the other hand, the DC bias routing design for RTAs, though critical in RTA design, is rarely discussed. The DC bias routing is an additional structure for RTAs, which affects the radiation performance, such as transmission coefficient and radiation pattern. Therefore, a further discussion on the DC bias routing design of RTAs is also included in this thesis.

1.3 Contribution

A 1-bit reconfigurable wideband PIN-diode-loaded unit cell is proposed, which achieves a 3-dB insertion loss bandwidth of 23.8% and a minimum insertion loss of 0.798 dB. Four PIN diodes are used in each unit cell and can be controlled at the same time using only one DC bias line, which greatly reduces the complexity of its DC routing design. Besides, the proposed unit cell remains a good operating bandwidth even with up to 40° oblique incidence. A prototype of the proposed unit cell is designed at X-band, fabricated, and tested using the waveguide measurement technique.

On the other hand, four designs of DC bias routing without using RF chokes are proposed. Two of them are based on the routing rules summarized from our literature survey, and the others are based on our advanced routing concept. To estimate the DC bias routing impact on the performance of the proposed RTA unit cell, two simulation methods are introduced, helping us to analyze the influence of different DC bias routing designs.

Limited by the fabrication cost, an 8×8 RTA prototype formed by the proposed unit cell along with the best of the four DC bias routing designs is fabricated and measured in the anechoic chamber. It shows a 3-dB gain bandwidth of 25% and 40° (2.3 dB) × 40°

doi:10.6342/NTU202302000

(3.3 dB) beam scanning range and loss in the two principal planes. Indeed, the agreement between the measured and simulated results verifies our design concepts.

1.4 Content Overview

In Chapter 2, we introduce the 1-bit reconfigurable unit cell structure in detail. The functions of each component are discussed, and also the logic behind our design. Furthermore, we compare the performance of the proposed unit cell with other related works.

In Chapter 3, the impact induced by DC bias routing is discussed. We summarize the previous works and acquire some routing rules, then we present a new routing principle to reduce the routing impact on a wideband unit cell. Besides, two estimation methods for the impact of DC bias routing are proposed, which help designers to preliminarily improve their DC bias routing design.

In Chapter 4, we use the waveguide measurement technique to measure the performance of our unit cell for verification. Also, an 8×8 RTA based on our unit cell and the DC bias routing design is fabricated and measured in the anechoic chamber. The reconfigurability of the unit cells is tested during the beam steering measurement.

In Chapter 5, as a conclusion, we summarize the results and discuss the future applications of our work.

doi:10.6342/NTU202302000

Chapter 2 1-Bit Reconfigurable PIN-Diode-Loaded Wideband Unit Cell

The proposed unit cell presented in this research is shown in Fig. 2.1, and its S-parameters are shown in Fig. 2.2. It is built upon the foundation in [13]. The proposed unit cell inherited its wideband characteristic and has been further developed to incorporate reconfigurability features. By integrating PIN diodes, the unit cell is capable of supporting 1-bit phase quantization. This chapter will begin with a brief overview of the unit cell introduced in [13], followed by a discussion of the improvements we have made.

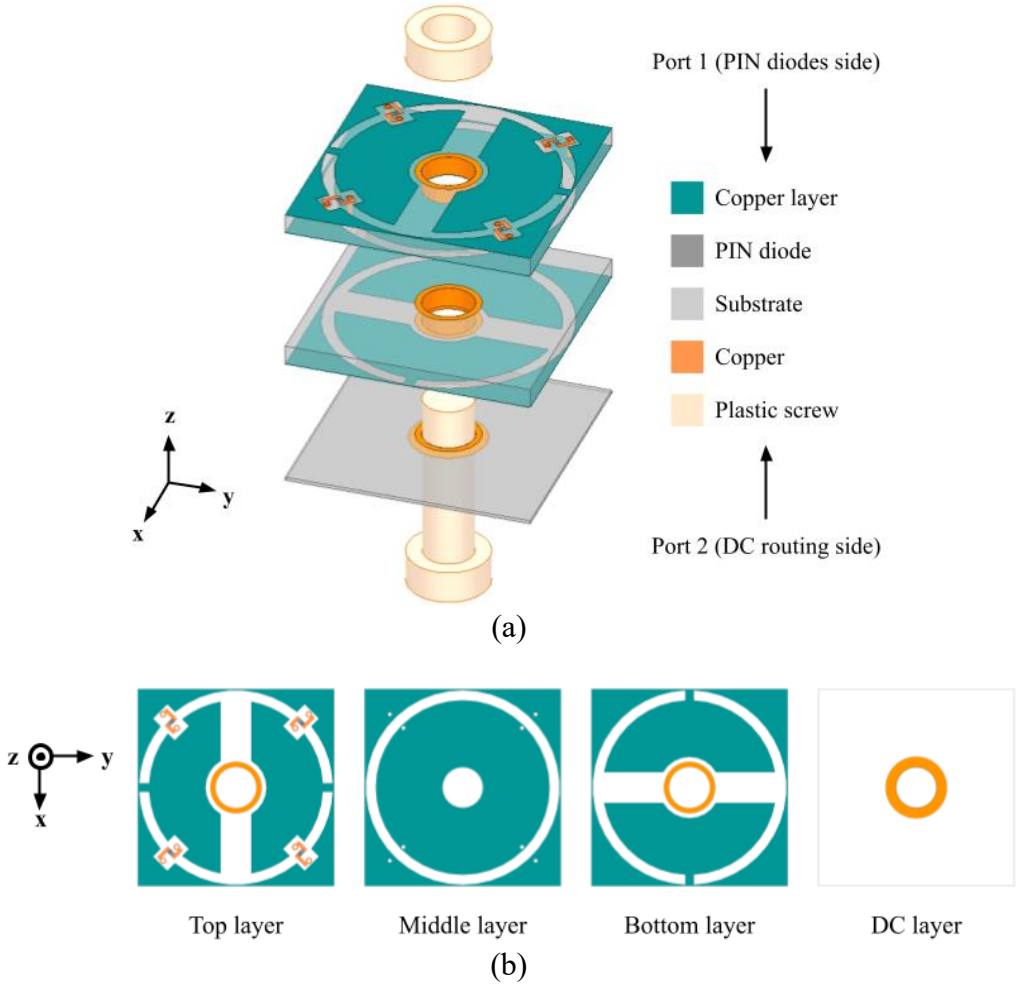

Fig. 2.1. Configuration of the proposed unit cell. (a) Trimetric view. (b) Top view of each

doi:10.6342/NTU202302000

layers.

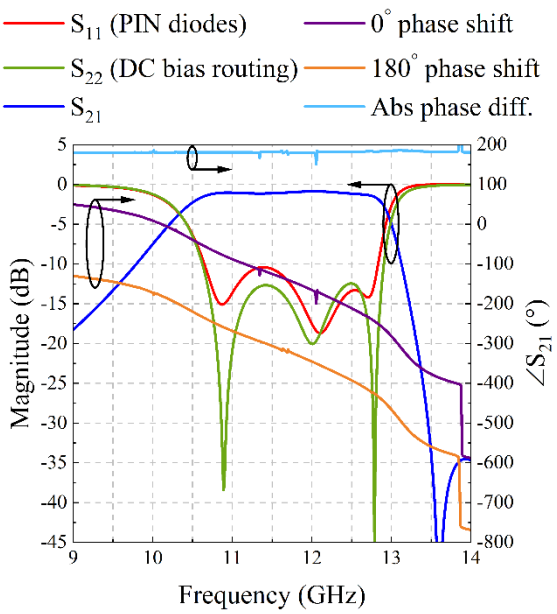

Fig. 2.2. The S-parameters of the proposed unit cell.

2.1 Adding PIN Diodes to Achieve Reconfigurability

The unit cell in [13] consists of two substrates and three copper layers. The substrates are Rogers R/T Duroid 5880 (ε = 2.2). Each copper layer has a cut slotted-ring aperture, which generates the boundary condition that the polarization will be perpendicular to the cut axis. From the top layer to the bottom layer, the apertures are orientated at 0°, ±45°, and 90°. Therefore, the unit cell in [13] performs polarization rotation by mutual coupling between layers. When an incident wave passes through the first aperture, the orientation of the aperture of the middle layer will decide the way of polarization rotation to be clockwise or counterclockwise. In [21], the modal expansion method (MEM) is applied, which indicates there are total of three resonant modes existing in the operating band.

doi:10.6342/NTU202302000

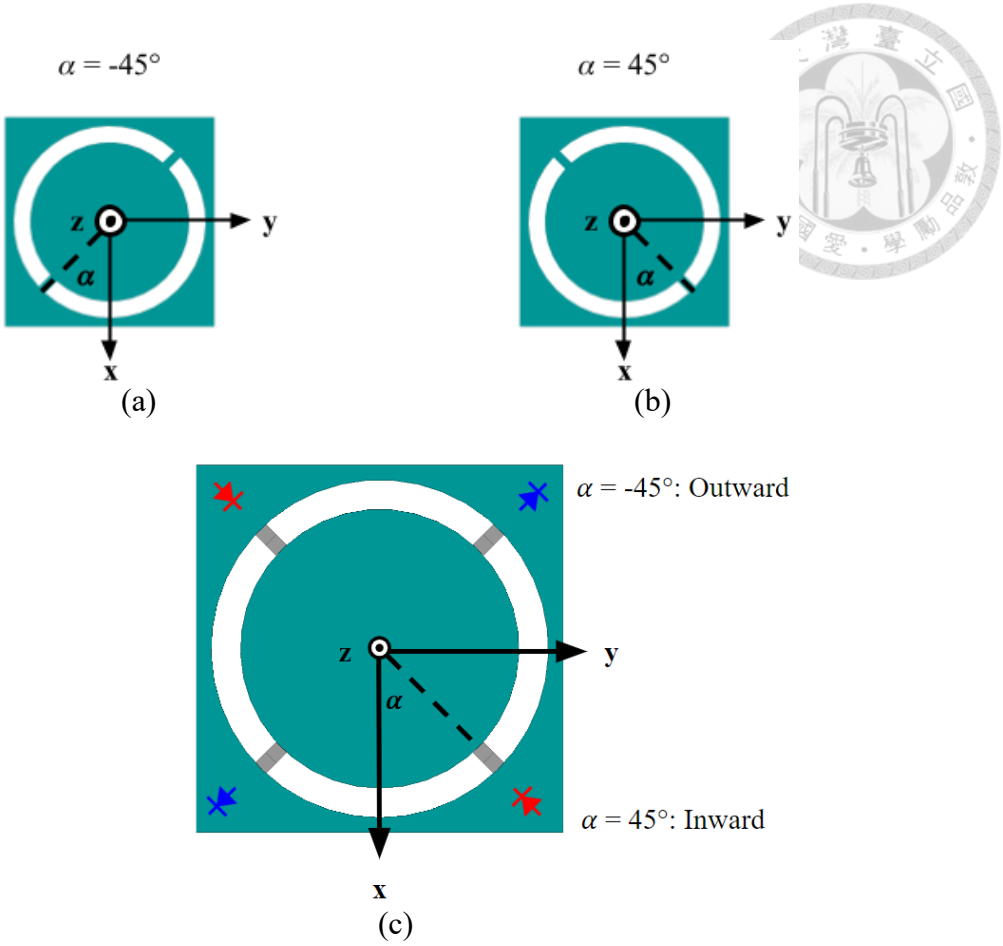

Fig. 2.3. The middle layer with cut at (a) α = -45°, (b) α = 45° and (c) combination.

The only difference between the 1-bit unit cell pair in [13] is the cut angle α at the middle layer, as shown in Fig. 2.3 (a)(b). The other parameters are all identical. Therefore, two PIN diode pairs are used to combine these two types of middle layers together, as shown in Fig. 2.3 (c). The PIN diode in use is MA4AGP907, whose equivalent RLC model of ON state and OFF state are shown in Fig. 2.4. Two PIN diode pairs are placed in the diagonal of the middle layer with different orientations. The blue pair is placed outward at α = -45°, while the red pair is placed inward at α = 45°. Due to the opposite placement, the state of both PIN diode pairs at different diagonals can be set differently at the same time. At the middle layer, the area outside the slotted ring is set to be GND. When the center area is positively biased, the blue PIN diode pair will be turned ON, and

doi:10.6342/NTU202302000

the red pair will be turned OFF at the same time, generating the cut at $\alpha = -45°$. Similarly, a negative bias at the center area will generate the cut at $\alpha = 45°$. In this way, both types of the middle layer can be electronically switched by assigning the center polarity, then get the reconfigurability.

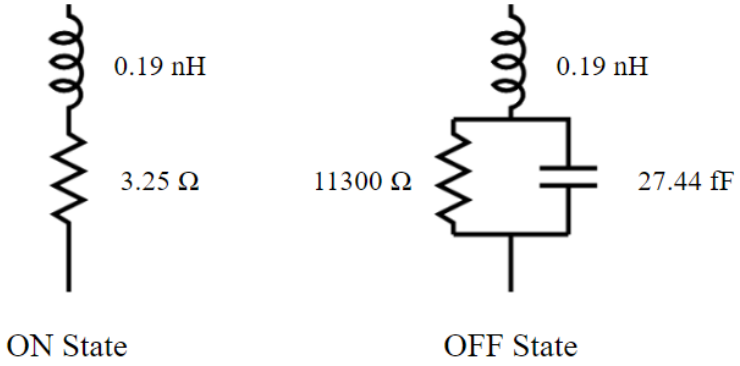

Fig. 2.4. Equivalent RLC models of MA4AGP907 PIN diode.

2.2 Loading Effect of PIN Diodes

On the cut slotted-ring aperture, the incident wave is rotated coupled start from the orthogonal axis of the cut, where is the ideal OPEN boundary. However, after the OPEN boundary is replaced with an OFF-state PIN diode, it becomes an imperfect OPEN. The S_{11} of each middle-stage unit cell is shown in Fig. 2.5. The OPEN boundary has zero capacitance, whereas an OFF-state PIN diode has a few capacitances. Thus, to reach the same impedance and satisfy the physical resonance in such aperture, the resonant frequencies are shifted to low-frequency region. Moreover, by comparing the electrical field distribution of each mode, the second mode is too close to the third mode, so they are combined into a single band.

doi:10.6342/NTU202302000

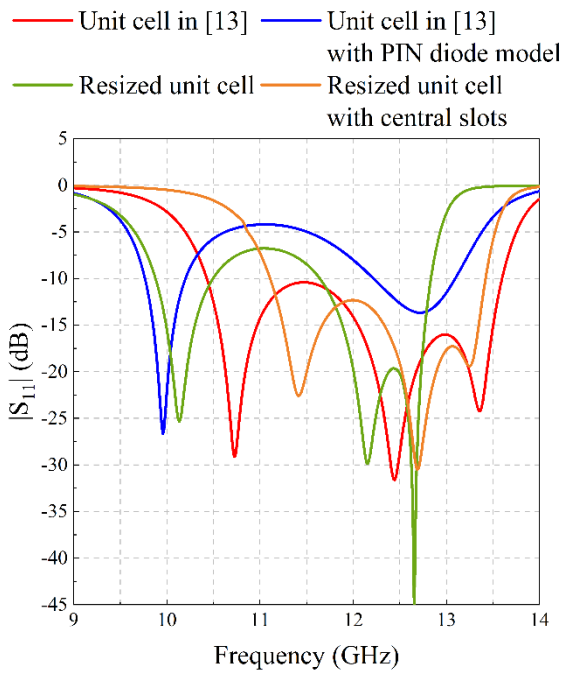

Fig. 2.5. The S_{11} of each middle-stage unit cell structure.

2.2.1 Resizing the Unit Cell

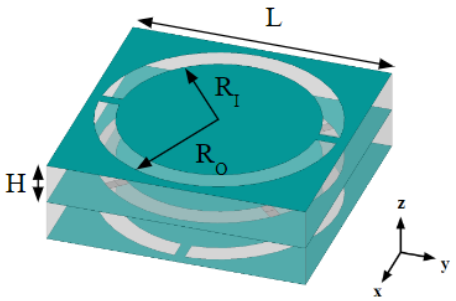

Fig. 2.6. The geometrical dimension of the unit cell.

The physical parameters of the unit cell are shown in Fig. 2.6. To deal with the loading effect of PIN diodes, a series of parametric studies are finished. The resized parameters are listed in Table 2.1. Among them, we reduce the substrate thickness, so that the new aperture will restore the second mode. However, the distance between the first mode and the other modes is still too far, forming two narrow operating bands whose reflection coefficient is less than -10 dB, as the orange curve shown in Fig. 2.5.

doi:10.6342/NTU202302000

Table 2.1. Comparison of physical parameters.

Parameters / Unit cell model	L (mm)	R_O (mm)	R_I (mm)	H (mil)
Unit cell in [13]	10	4.6	3.8	62
Resized unit cell with PIN diode models	9.6	4.75	4.25	31

2.2.2 Adding Central Slots

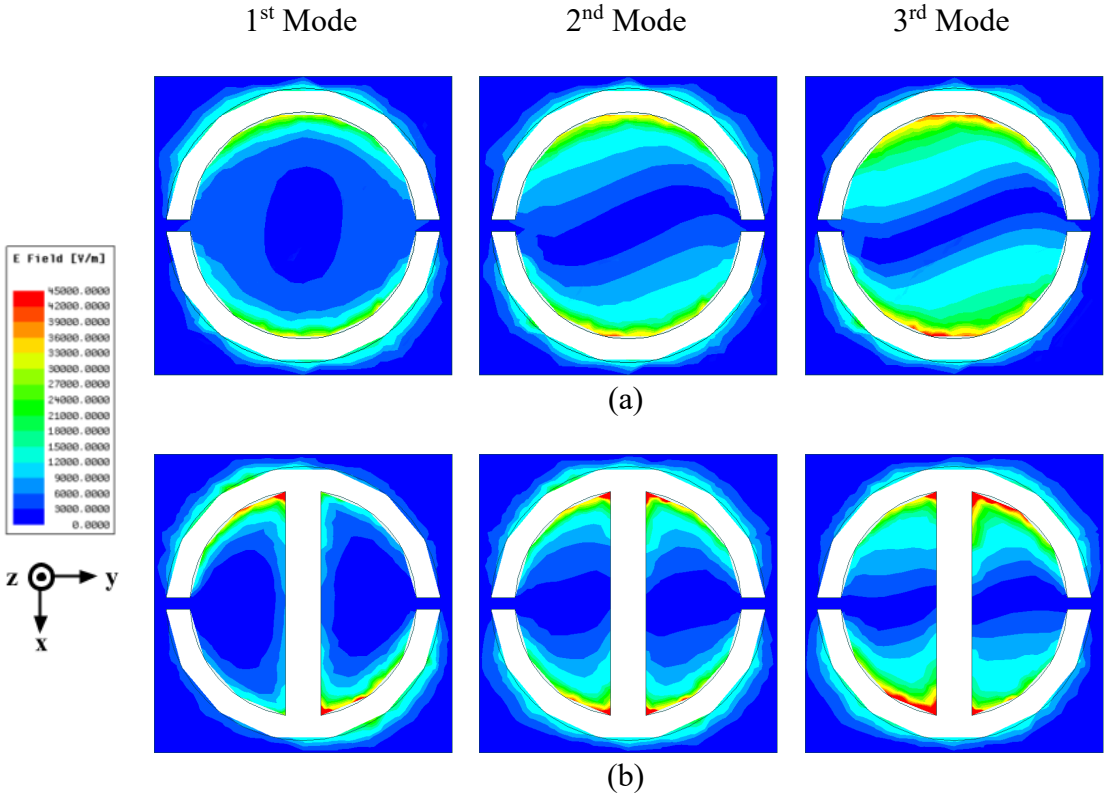

Fig. 2.7. Electric fields distribution of three resonant modes on the top layer of [13] (a) without and (b) with central slots.

Here, the central slots are added on the top and the bottom layer, whose orientations are parallel to the corresponding polarization, so that they have little effect on original resonant modes. Preliminary validation of the central slots has been done by using the passive unit cell in [13]. The electric field distribution of three resonant modes on the top layer are shown in Fig. 2.7. These central slots can destroy the electric field distribution

doi:10.6342/NTU202302000

at the middle of the top and the bottom layers. Therefore, the resonances will be started from the edges of the central slots, as the yellow arrows shown in Fig. 2.8.

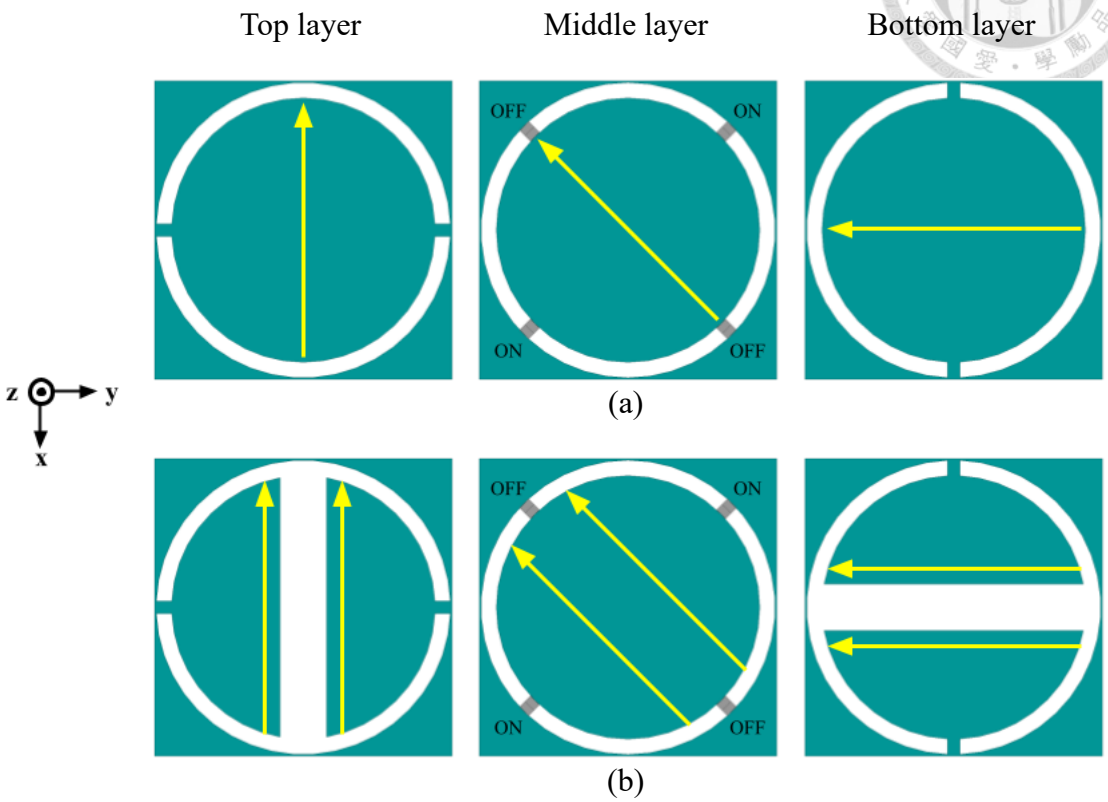

Fig. 2.8. Main resonant area in the resized unit cell (a) without and (b) with central slots.

After the rotated coupling to the middle layer, the OPEN boundary is now moved to the left-hand side and right-hand side of the OFF-state PIN diodes, which are more like an ideal OPEN. Therefore, the resonant frequencies are shifted back to high-frequency region and become close to each other, which forms a single wide operating band, as the green curve shown in Fig. 2.5. Compared with the passive unit cell in [13], the bandwidth becomes narrower. However, it is worth having the reconfigurability while reducing some bandwidth.

2.3 Fabrication Consideration

In the previous simulation, the RLC models of the PIN diode are directly placed at

doi:10.6342/NTU202302000

the middle layer. However, considering the fabrication, PIN diodes cannot be mounted in the middle of substrates. Therefore, PIN diodes need to be mounted on the top layer. Besides, an additional DC layer and a DC bias via for the center bias control are also needed. Now the unit cell structure is asymmetric, which can be defined as Port 1 (PIN diode side) and Port 2 (DC bias routing side). The S_{11} and S_{22} are shown in Fig. 2.9.

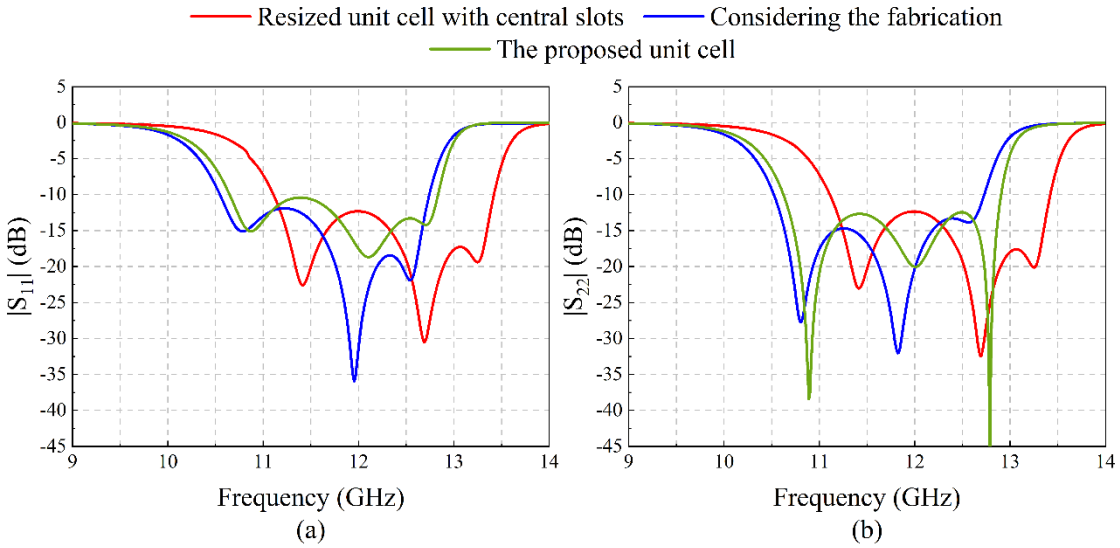

Fig. 2.9. The (a) S_{11} and (b) S_{22} of each middle-stage unit cell structure considering the fabrication process.

doi:10.6342/NTU202302000

2.3.1 Locations for Loading PIN Diodes and DC Layer

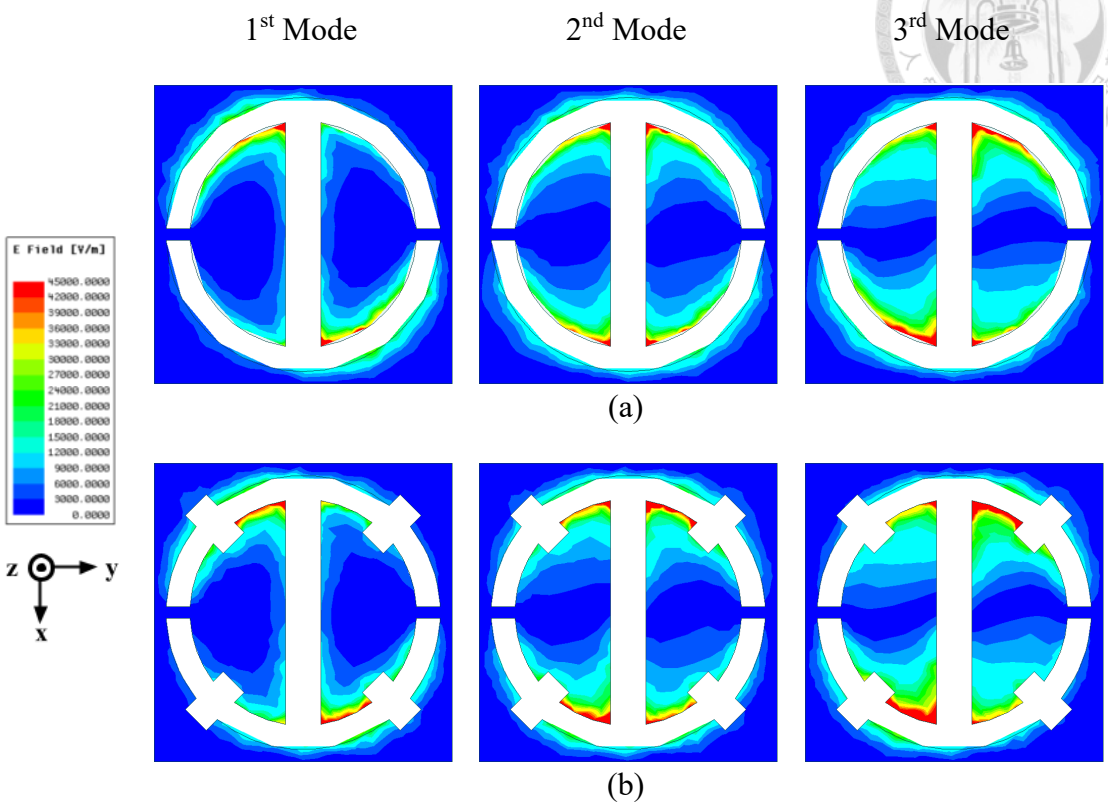

Fig. 2.10. Electric fields distribution of three resonant modes on the top layer of [13] (a) without perturbations, and (b) with perturbations.

Four perturbations are added at the diagonal of the top layer, leaving space for PIN diodes needed. Again, a preliminary simulation using the passive unit cell of [13] has been done. The electric field distribution on the top layer after adding perturbations is shown in Fig. 2.10 (b). The influence of perturbations can almost be neglected. On the other hand, the length of PIN diodes is almost equal to the width of the cut slotted ring, which will cause some fabrication inconvenience. Therefore, PIN diodes are placed tangent to the slotted ring. Since PIN diodes are placed on the top layer, the DC substrate with a center via is added below the bottom layer, whose thickness is 5 mils. The unit cell structure modified from [13] was previously published in [20], as shown in Fig. 2.11.

doi:10.6342/NTU202302000

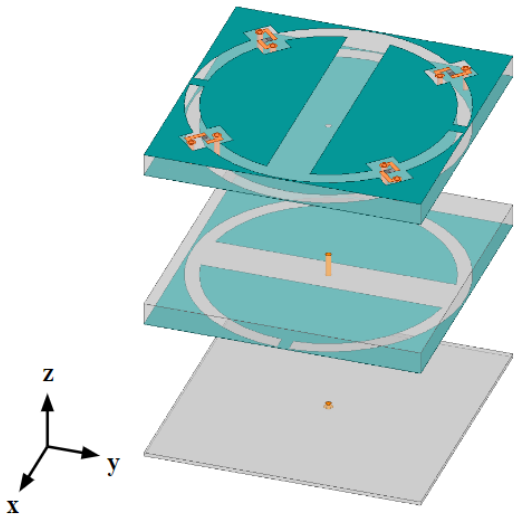

Fig. 2.11. The unit cell structure previously proposed in [20].

The S-parameters of the unit cell proposed in [20] are the blue curves shown in Fig. 2.9. While PIN diodes are being placed on the top layer, the OPEN boundary at the middle layer has been changed. The OFF-state PIN diode with some metal connection is still a capacitive loading, and the vias for PIN diodes connection can be treated as a transmission line, whose length is approximately 0.035λ to 0.055λ inside Rogers RT/Duroid 5880 substrate. Therefore, the capacitance seen from the middle layer is increased, then the resonant frequencies are shifted to low-frequency region.

2.3.2 Plastic Screw for Substrates Combination

Since the cooperated PCB factory didn't provide a suitable tape to combine substrates together, the unit cell structure we previously proposed in [20] needs to be modified. To make sure the conduction between the DC bias via and the middle layer, the DC bias via is enlarged and becomes a screw hole, where an M2 screw is passing through to lock all substrates together. Because the size of the screw is close to the unit cell, the material of the screw is chosen to be plastic ($\varepsilon = 3.5$) but not metal, which may cause additional strong radiation. In this way, the pad ring of the enlarged DC bias via in each

doi:10.6342/NTU202302000

substrate will touch together and then connect to the center area of the middle layer. Compared with the unit cell previously proposed in [20], the reflection in high-frequency region is increased. It is because the center area contributes to the higher modes as discussed before.

2.4 Oblique Incidence Influence

The proposed unit cell can be used to beam steering applications. Since the excitation of beam steering setup is usually a spherical wave but not a plane wave. Therefore, the oblique incidence is an important issue to be discussed. In our case, the phase difference between the proposed 1-bit unit cell pairs is unaffected due to the robustness of the physical polarization rotation mechanism. Thus, the oblique incidence influence is focused on the magnitude of the S-parameters, which are shown in Fig. 2.12. The 3-dB insertion loss bandwidth is almost unchanged with the oblique incident angle up to 40° in both principal planes. The most obvious impact is the increasing insertion loss near 11.5 GHz and 12.5 GHz, which is less than 0.5 dB. A brief summary is that the proposed unit cell is slightly sensitive to the oblique incidence angle and remains the wideband characteristic.

doi:10.6342/NTU202302000

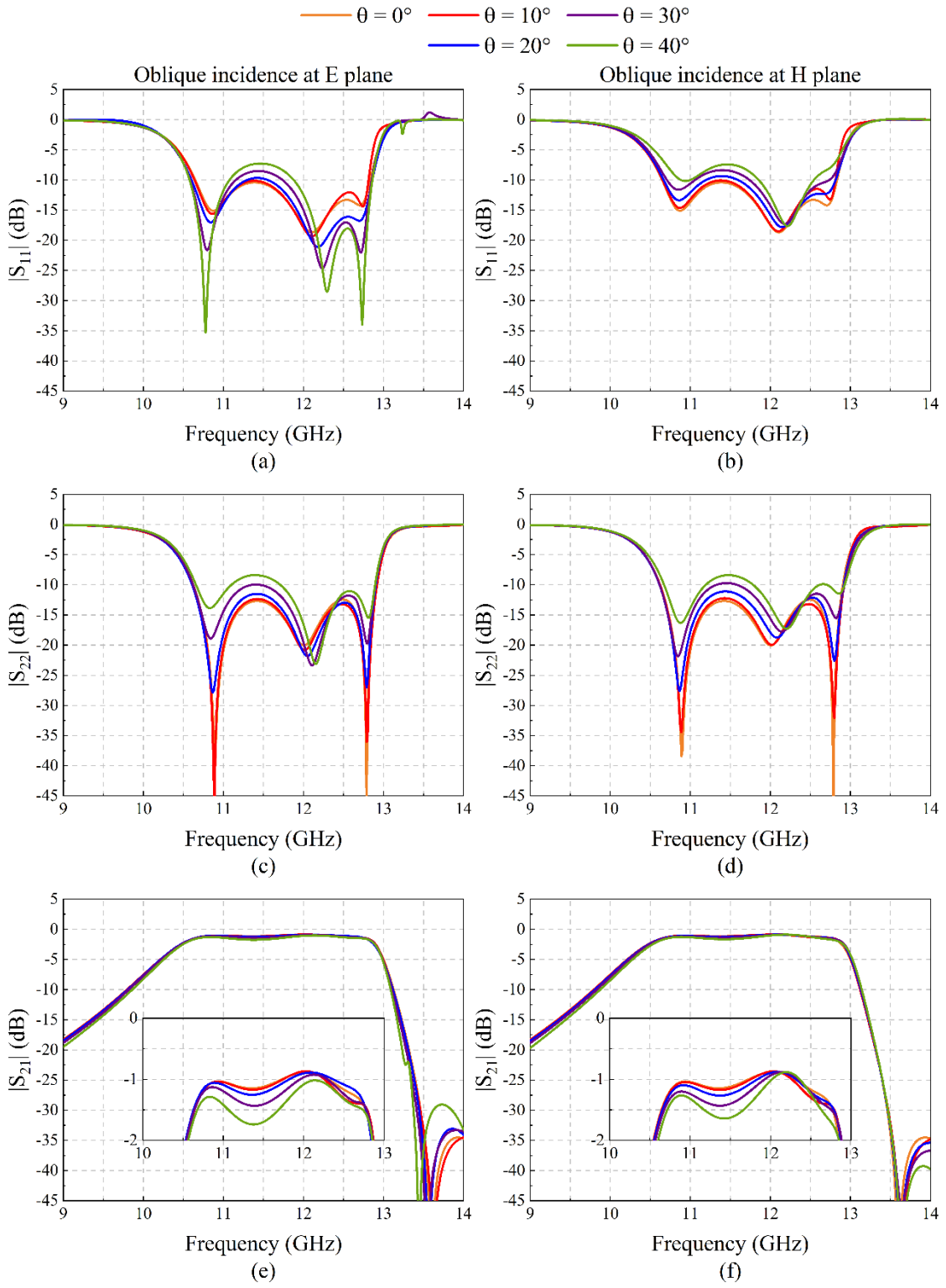

Fig. 2.12. The S-parameters of the proposed unit cell with oblique incidence from θ = 0° to 40° at (a)(c)(e) E plane and at (b)(d)(f) H plane.

doi:10.6342/NTU202302000

2.5 Comparison with Other Works

After all the modifications mentioned above, the proposed unit cell is compared with other 1-bit reconfigurable unit cells based on generating opposite polarization. The important indexes are summarized in Table 2.2. The proposed unit cell has the 3-dB insertion loss bandwidth of 23.8% and the minimum insertion loss of 0.798 dB. The values in the brackets are the results from [20], which is the ideal case. Compared with [8], [10], and [11]. this work has a wider 3-dB insertion loss bandwidth and a smaller minimum insertion loss. When comparing with [12] and [19], this work is a trade-off between the bandwidth and the minimum insertion loss. However, an air layer is used in their unit cell, which increases the fabrication complexity, while the proposed unit cell features a simple structure.

Table 2.2. Comparison with other 1-bit reconfigurable unit cells based on generating opposite polarization.

Reference	Frequency (GHz)	Lattice size (λ_c)	3-dB IL BW (%)	Minimum IL (dB)	Substrate (#)
[8]	10.5	0.53	7.6	1.8	3
[10]	29	0.49	11.2	1.09	3
[11]	10	0.5	14.7	1.87	3
[12]	12.5	0.5	16	0.47	5 (1 air)
[19]	11.5	0.58	26	1	3 (1 air)
This work	**11.5**	**0.368**	**23.8 (22.2)**	**0.798 (0.753)**	**3**

doi:10.6342/NTU202302000

Chapter 3 Discussion on DC Bias Routing Design

For an RTA, it is necessary to additionally design its DC bias routing to control the active elements. In recent years, there have been many studies on RTA, which mentioned some related DC bias routing designs, but there are no in-depth discussions on how to design them.

In unit cell designs of RTAs, the Rx-Tx-based designs separate the antennas of the receiving end and the transmitting end and separate them with metal to allow signals to be transmitted through via holes. Under such configuration, the DC bias routing can be well hidden between the metal layers or has a negligible effect even placed near its receiver or transmitter. On the other hand, the FSS-based designs usually have polarizer layers, which can be used as its DC bias routing at the same time.

However, for the FSS-based designs without polarizer layers, there is nowhere for DC bias routing to hide. Its DC bias routing will be directly added to the surface of RTA, which will inevitably affect the transmission performance.

On the other hand, to isolate the DC and RF signals in a large RTA, an excessive number of discrete components are needed. The fabrication cost and the DC bias routing design complexity in limited space will be significantly increased.

In this chapter, the discussion is mainly for the FSS-based RTAs without polarizer layers under the constraint of not using discrete components for DC and RF isolation, aiming to obtain the related advanced DC bias routing design guidelines.

doi:10.6342/NTU202302000

3.1 Basic Rules of DC Bias Routing

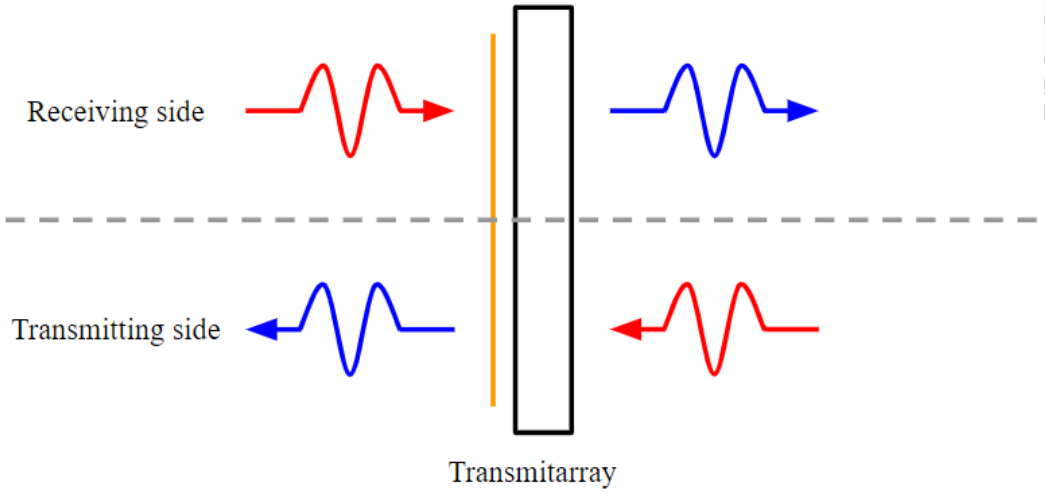

Fig. 3.1. Sketch of the roles of the DC bias routing surface.

In the literature survey, we have summarized these DC bias routing designs, and we can get some basic rules that everyone abides by. As shown in Fig. 3.1, an RTA is a bidirectional structure, so the DC bias routing sometimes acts as a receiving surface and sometimes as a transmitting surface. In Table 3.1, the basic DC bias routing rules corresponding to the routing problems are organized.

Table 3.1. Summary of basic DC bias routing rules for all RTAs.

The Source Blocking	**The Modal Deterioration**
1. Be perpendicular to the feed polarization.	2. Avoid the strong field area.
3. Minimize the routing area.	

3.1.1 Rule 1 — Be Perpendicular to the Feed Polarization (The Source Blocking)

When the DC bias routing is used as the receiving surface, the DC bias routing is the first structure encountered by the incident wave. There may be as many as hundreds of DC bias routing on an RTA, so it is likely to block the incident wave. In other FSS-based

doi:10.6342/NTU202302000

designs with polarizer layers, it can be found that their DC bias routing is designed parallel to their polarizers. Therefore, for the FSS-based designs without polarizer layers, the DC bias routing should be designed along the direction perpendicular to the polarization of the incident wave. When hundreds of lines are stacked along this direction, it is equivalent to seeing a polarizer for the incident wave, so its blocking effect can be minimized.

3.1.2 Rule 2 — Avoid the Strong Field Area (The Modal Deterioration)

The FSS-based designs are able to perform multi-layer coupling to transmit EM wave signals. However, for the FSS-based designs without polarizer layers, their DC bias routing on the RTA surface may cover resonant apertures. Therefore, fractions of DC bias routing on each unit cell of RTA should be considered as part of the unit cell antenna.

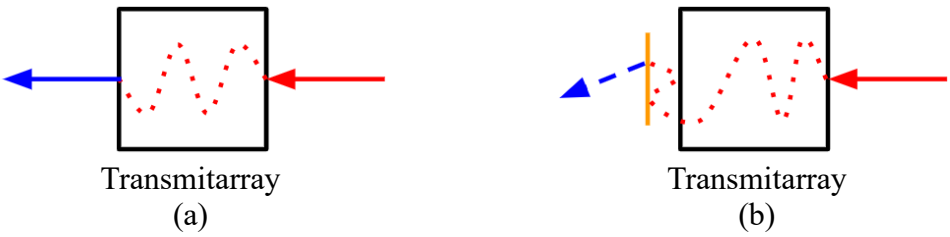

Fig. 3.2. Sketch of (a) original mode and (b) deteriorated mode.

Whether the DC bias routing is used as the transmitting surface or receiving surface, the EM wave needs to pass through the additional DC bias routing structure before forming the resonance inside the original aperture. There are usually one or more resonant modes within the operating band, and these modes generate stronger fields at certain coupling locations on the unit cells. When DC bias routing passes through these resonance regions, the modal deterioration is more likely to occur, as illustrated in Fig. 3.2. Intuitively speaking, the design of DC bias routing should try to avoid passing through these modal resonance locations.

doi:10.6342/NTU202302000

3.1.3 Rule 3 — Minimize the DC Bias Routing Area

In addition to the above two types of problems, since the DC bias routing is an additional structure, the simpler and more direct the design, the smaller the DC bias routing area, the better. Taking an 8×8 RTA as an example, a direct and simple DC bias routing design is shown in Fig. 3.3 (a). It can be seen that all lines extend to the right-hand side of the RTA, and the longest line length is 8 units. In Fig. 3.3 (b), under the same design logic, half of the lines are extended to the left of the RTA, and the other half is extended to the right of the RTA. In this way, the length of the longest line is halved to 4 units. In addition, in the application of beam steering, the incident wave of RTA is a relatively short-distance spherical wave, and the unit cells in the middle of the RTA have a greater impact on the overall performance than the unit cells at the edge of the RTA. A balanced design can not only halve the length of the DC bias routing but also minimize the DC bias routing area in the middle of RTA. Furthermore, it can make the radiation pattern more symmetrical.

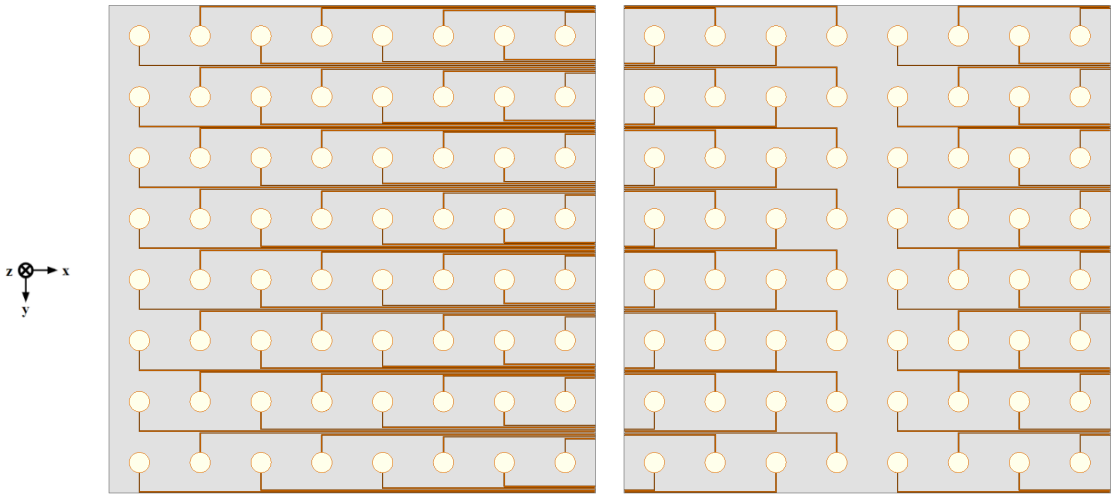

(a) (b)

Fig. 3.3. The 8×8 RTA with (a) all DC bias routing extend to the right-hand side, and with (b) DC bias routing extend to both sides evenly.

doi:10.6342/NTU202302000

3.2 DC Bias Routing Design Strategies

In the proposed unit cell structure, the DC bias routing layer is located under the bottom layer. Here, for the convenience of observation, the diagram is rotated upside down. In this section, different DC bias routing designs and the design logic behind them are discussed.

3.2.1 Following the Basic Rules — Case 1 and Case 2

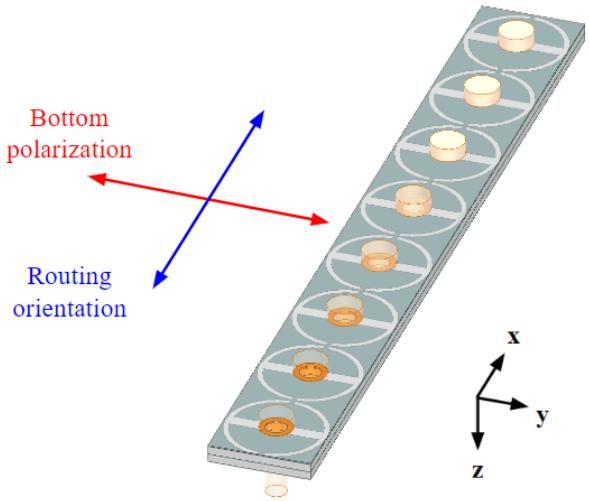

Fig. 3.4. Indication for routing orientation.

Case 1 and Case 2 follow the basic rules. First, the bottom layer is polarized along the y-axis, so the DC bias routing should run towards the x-axis, as shown in Fig. 3.4. Second, the proposed unit cell has three resonant modes, whose electric field distribution at the bottom layer is shown in Fig. 3.5, including (a) 0° phase shift and (b) 180° phase shift. If the 1-bit unit cell pairs are considered together, the electric field is mainly distributed symmetrically at the cut slotted ring, and it is distributed toward the center of the unit cell when higher modes occur. As discussed in subsection 2.2.2, the mutual coupling starts from the edge of the central slots. Therefore, regardless of modes, the

doi:10.6342/NTU202302000

electric field strength at the center of the central slot, four corners, and the middle area of the unit cell are relatively low, so the DC bias routing should be placed on these areas.

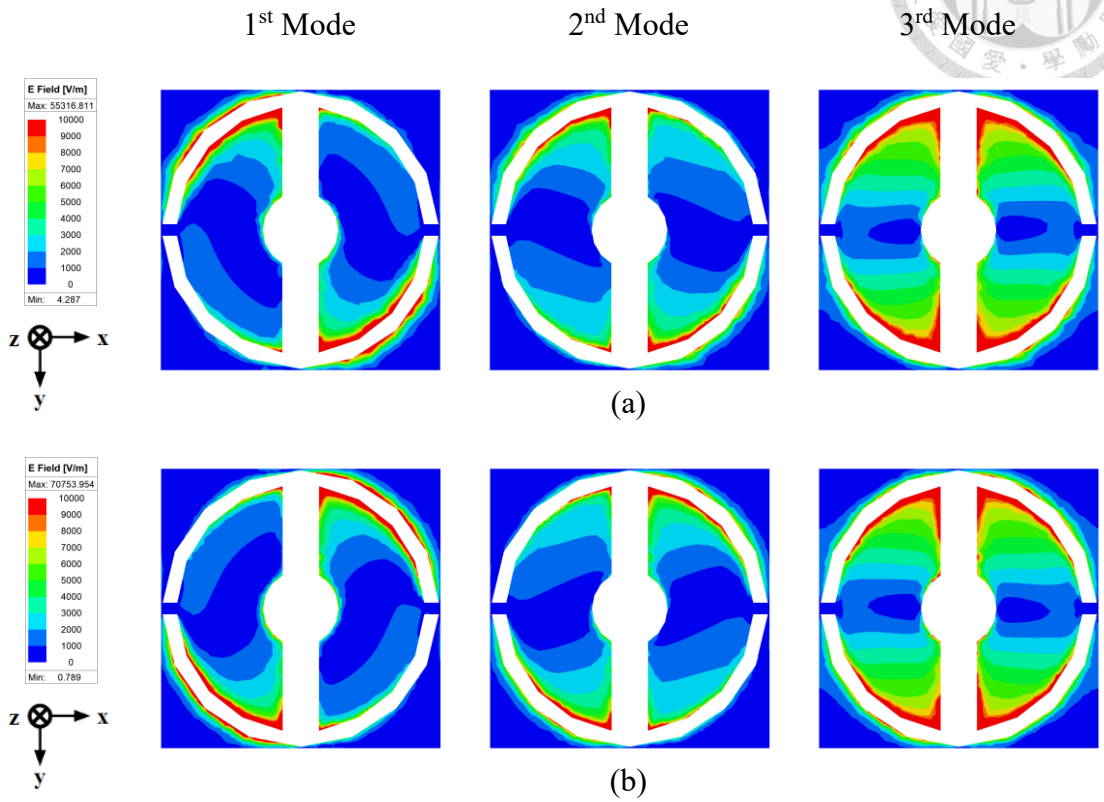

Fig. 3.5. Electric fields distribution of three resonant modes on the bottom layer of (a) 0° phase shift unit cell, and (b) 180° phase shift unit cell.

Since the distribution of the field is center-symmetric in the proposed unit cell, the DC bias routing should be evenly distributed on both sides of the unit cell to maintain a symmetrical radiation pattern. Besides, as shown in Fig. 3.6, for DC bias routing in the same length (e.g. 8 units), the DC bias routing placed (a) at the same side of the unit cell is much close to the center of the unit cell than that placed (b) at both sides of the unit cell, which will limit the array size.

doi:10.6342/NTU202302000

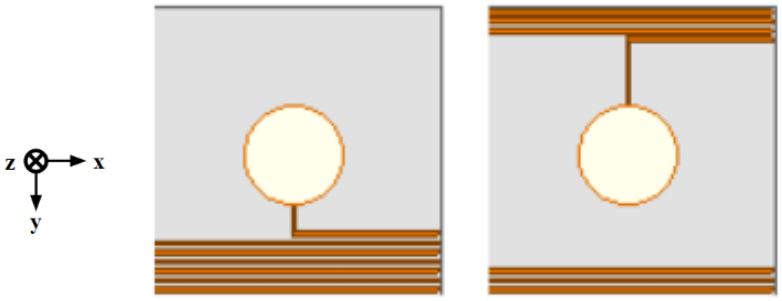

(a) (b)

Fig. 3.6. The edge unit cell in the 16×16 RTA with 8-unit long DC bias routing placed at (a) the same side of the unit cell, or (b) both sides of the unit cell evenly.

The DC bias routing design of Case 1 is shown in Fig. 3.7 (a), where the DC bias routing is started from the center of the central slot and evenly distributed along the edges on both sides of the unit cell. The DC bias routing area is reduced by a straight-line design. On the other hand, the DC bias routing design of Case 2 is shown in Fig. 3.7 (b). Its DC bias routing is evenly distributed along both sides of the center of the unit cell. Because the DC bias via is at the middle, although Case 2 is mainly a straight-line design, it is necessary to add an arc when passing through the center to avoid the DC bias via of other unit cells.

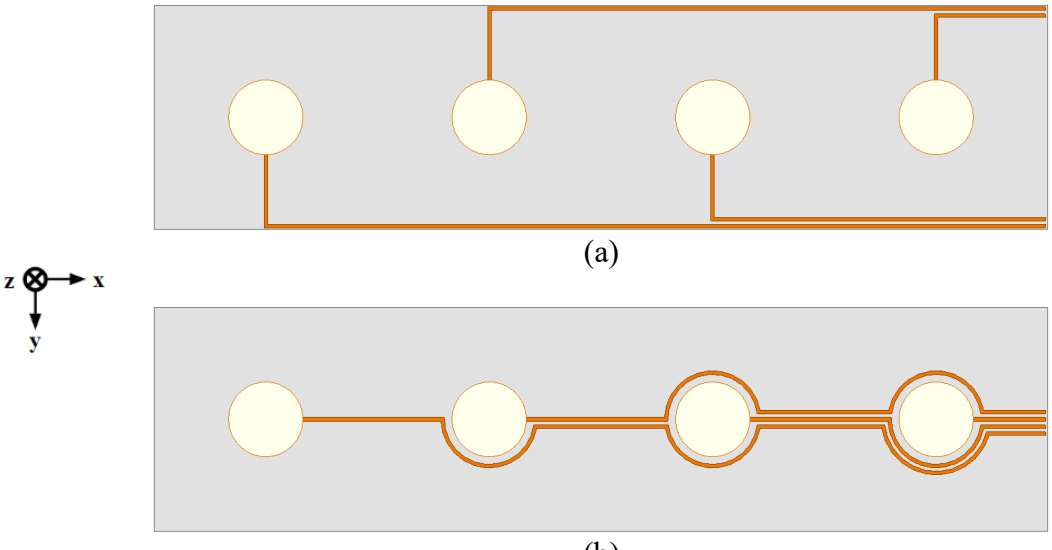

(a)

(b)

Fig. 3.7. Basic DC bias routing designs. (a) Case 1. (b) Case 2.

doi:10.6342/NTU202302000

3.2.2 Minimizing and Dispersing the Modal Deterioration Area of Each Mode — Case 3 and Case 4

It can be known that even if the DC bias routing extends along the weaker field area when the RTA gradually expands, the unit cells near the edge of RTA will still be affected by the increase in the number of stacked DC bias routing. Since the proposed unit cell is a wideband design, there are three resonant modes, and there are relatively many areas where resonance occurs on the unit cell, so piles of DC bias routing will inevitably affect at least one mode, then cause the modal deterioration problem. For example, as shown in Fig. 3.8 (a)(b), the DC bias routing design of Case 1 is mainly in the area on both sides of the unit cell. When the RTA becomes larger (e.g. 16×16), the main resonance area of lower modes will be covered. Similarly, the DC bias routing design of Case 2 is mainly in the middle of the unit cell, and when the RTA becomes larger, higher modes across the central area will start to be affected, as shown in Fig. 3.8 (c)(d).

doi:10.6342/NTU202302000

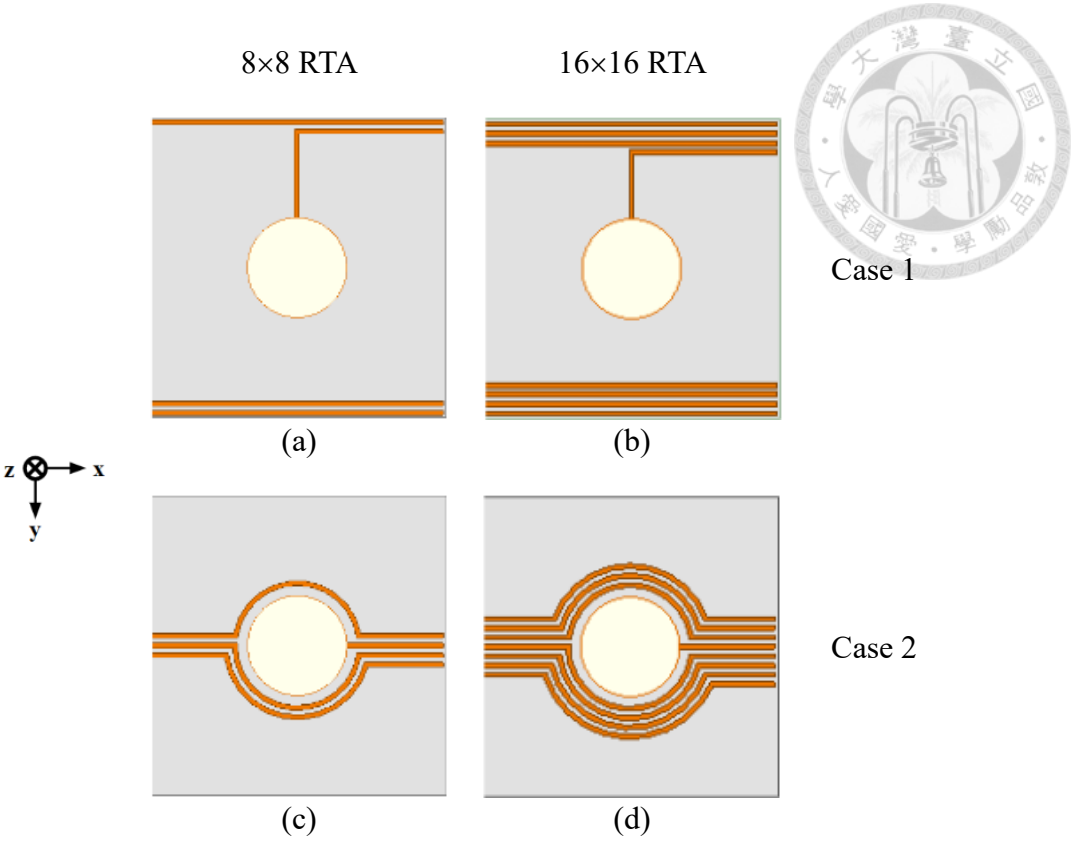

Fig. 3.8. Edge unit cell with Case 1 design in (a) the 8×8 RTA and (b) the 16×16 RTA, and with Case 2 design in (c) the 8×8 RTA and (d) the 16×16 RTA.

The modal deterioration happens on every covered unit cell of the RTA. As shown in Fig. 3.9 and Fig. 3.10, the blue area is the area where the lower modes are affected, and the red area is the area where the higher modes are affected. For Case 1 and Case 2, when the RTA expands, the transmission of some modes will be blocked, because the affected area covers almost the entire RTA. On the other hand, since we don't consider the usage of discrete components for isolation of DC and RF signals, the modal deterioration problem has a high possibility to lead the RF signal leakage along DC bias routing. The isolation between DC and RF signals will be terrible when almost the entire DC bias routing is coupled with RF signals.

doi:10.6342/NTU202302000

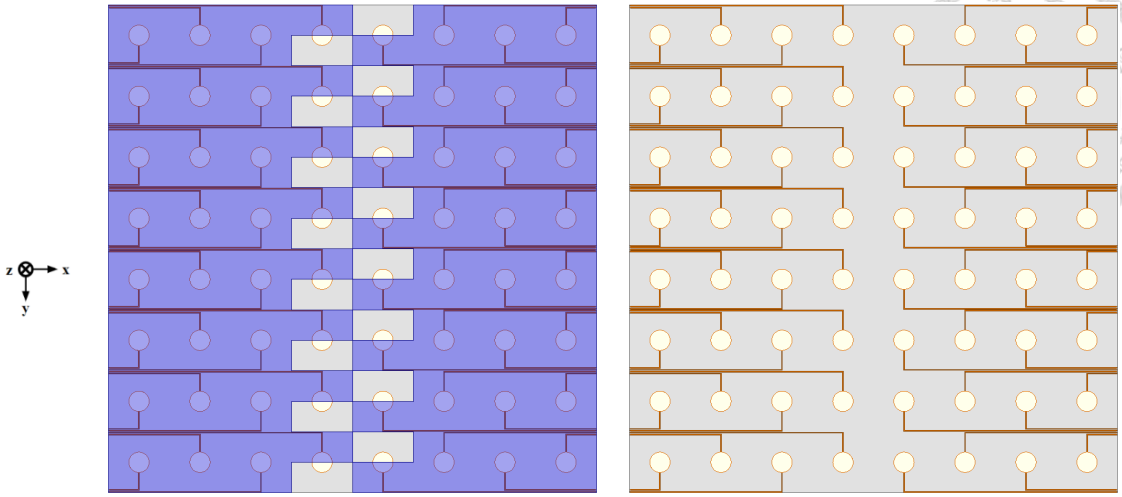

(a) (b)

Fig. 3.9. The affected area of (a) lower modes (colored in blue) and (b) higher modes (colored in red) in the 8×8 RTA with Case 1 DC bias routing design.

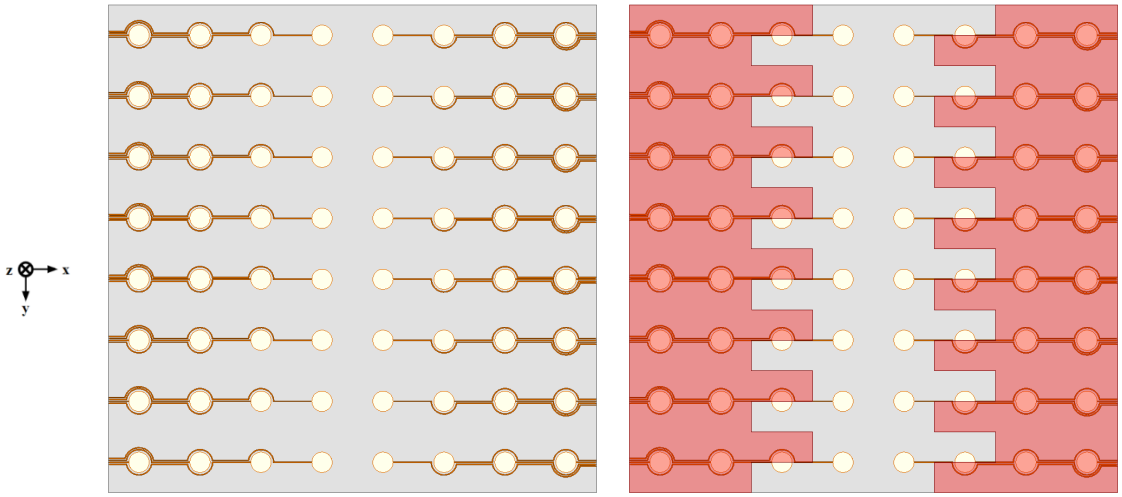

(a) (b)

Fig. 3.10. The affected area of (a) lower modes (colored in blue) and (b) higher modes (colored in red) in the 8×8 RTA with Case 2 DC bias routing design.

In order to solve the transmission blockage problem caused by the coverage of DC bias routing on a large, multi-mode RTA, we propose an advanced DC bias routing rule of "Minimizing and dispersing the modal deterioration area of each mode". The concept is to prevent the modal deterioration areas from being too concentrated by dispersing the

doi:10.6342/NTU202302000

affected areas into small pieces. When these affected small areas are distributed in chaos on the RTA, the transmission blockage problem can be alleviated.

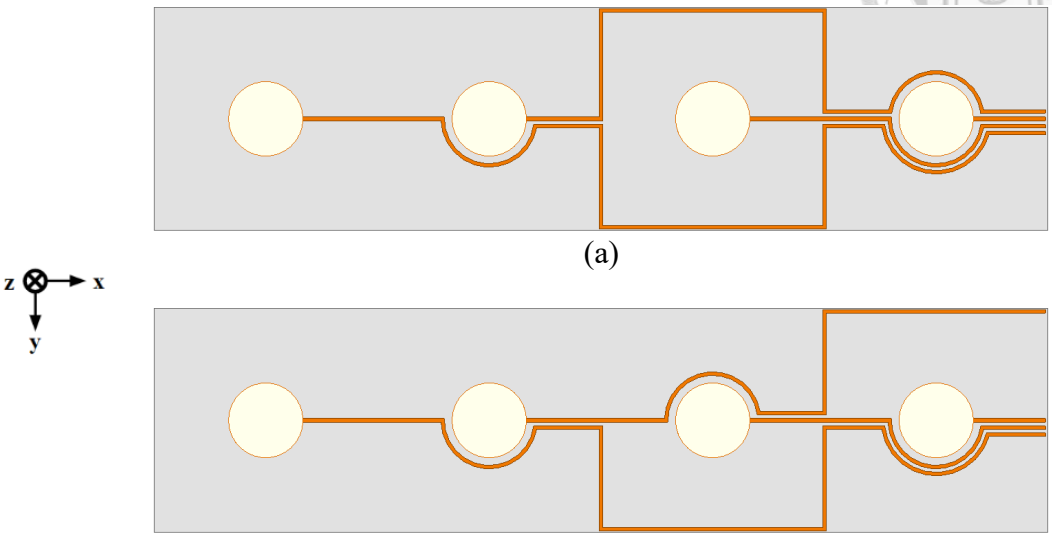

(a)

(b)

Fig. 3.11. Advanced DC bias routing designs. (a) Case 3. (b) Case 4.

According to the proposed advanced rule, Case 1 and Case 2 are mixed to get the novel designs, as shown in Fig. 3.11, Case 3 is the two cases mixed in the same order on both sides of the unit cell, and Case 4 is the two cases mixed in the opposite order on both sides of the unit. The affected area of each mode are shown in Fig. 3.12 and Fig. 3.13. Case 3 reduces the maximum affected area of each mode to a column size equivalently and separates them by modes. Whereas Case 4 further reduces the maximum affected area to almost half a unit cell, which is equivalent to a grid for both lower modes and higher modes. In this way, the large united affected area on the RTA becomes small and dispersed, which can improve the isolation issue and the transmission blockage when the size of the RTA increases.

doi:10.6342/NTU202302000

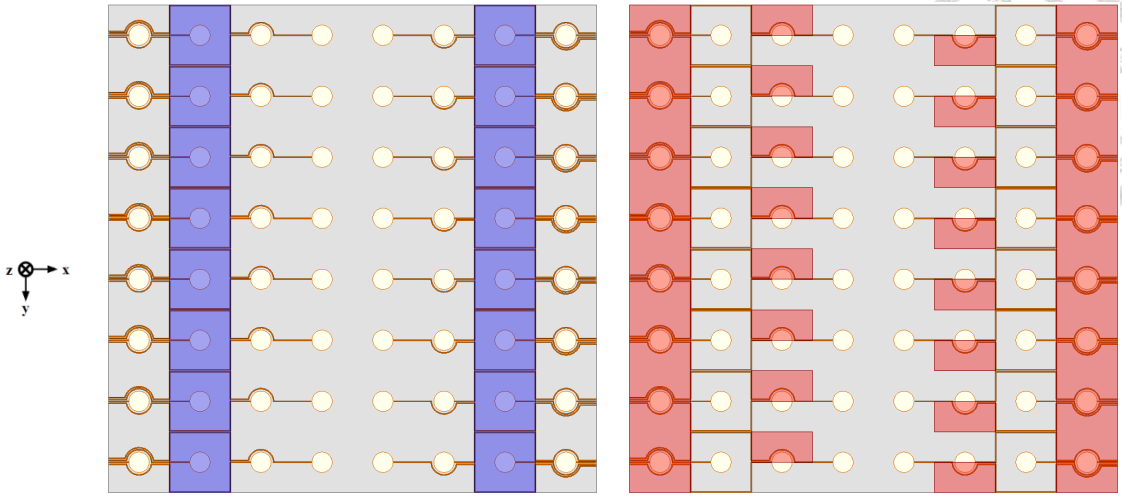

(a) (b)

Fig. 3.12. The affected area of (a) lower modes (colored in blue) and (b) higher modes (colored in red) in the 8×8 RTA with Case 3 DC bias routing design.

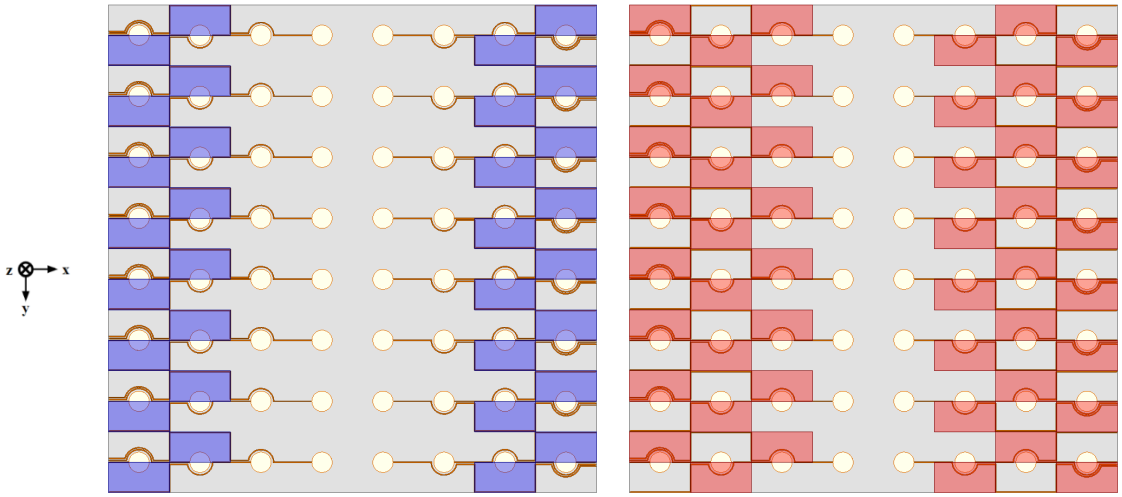

(a) (b)

Fig. 3.13. The affected area of (a) lower modes (colored in blue) and (b) higher modes (colored in red) in the 8×8 RTA with Case 4 DC bias routing design.

3.3 Methods to Estimate DC Bias Routing Impact

In the design process of RTAs, people usually use the periodic boundary condition (PBC) to design their antenna unit cells, and then add DC bias routing when expanding into an RTA. As discussed before, DC bias routing will induce some problems, such as

doi:10.6342/NTU202302000

modal deterioration, terrible isolation, and transmission blockage. In order to understand the transmission quality of RTA using different DC bias routing designs, the following methods are used to initially estimate the impact of the DC bias routing.

3.3.1 Scattered Fields Simulation

RTAs can be used to receive plane wave signals from far away. In HFSS, "Incident wave excitation" can be used to add plane wave excitation. The plane wave generated by using this setting has an infinite range. It is usually used in HFSS to simulate the scattered fields problem of finite-sized metal structures. In HFSS, the observation of scattered fields can be specified. Unlike the free space wave method, the resulting scattered fields will include the diffracted fields because of the infinite range of the excited plane wave. So it is difficult to resolve the radiated fields in the scattered fields. Benefiting from the concept of polarization rotation, the polarization direction of the diffracted fields and the radiated fields are orthogonal in this work, as shown in Fig. 3.14. Therefore, as long as the polarization direction corresponding to the radiated fields is selected, the radiated fields can be preliminarily resolved from the entire scattered fields.

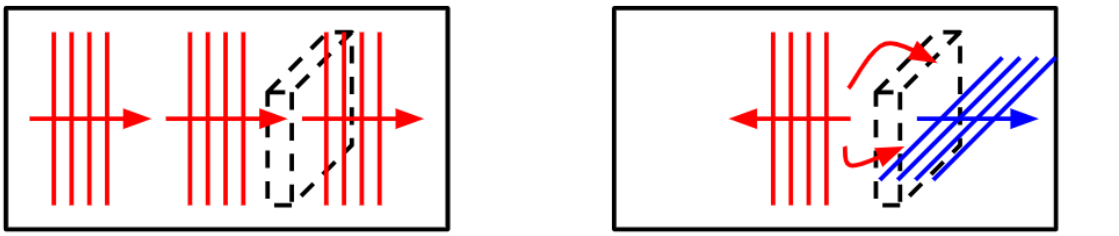

Fig. 3.14. Sketch of the scattered fields simulation.

Considering hardware resources, an 8×8 RTA is simulated. As shown in Fig. 3.15, the length of the DC bias routing is 4 units, and the corresponding polarized plane waves

doi:10.6342/NTU202302000

are excited on both sides of the RTA. Each unit cell on the RTA is excited with the same magnitude and phase, so each unit cell contributes the same proportion to the RTA.

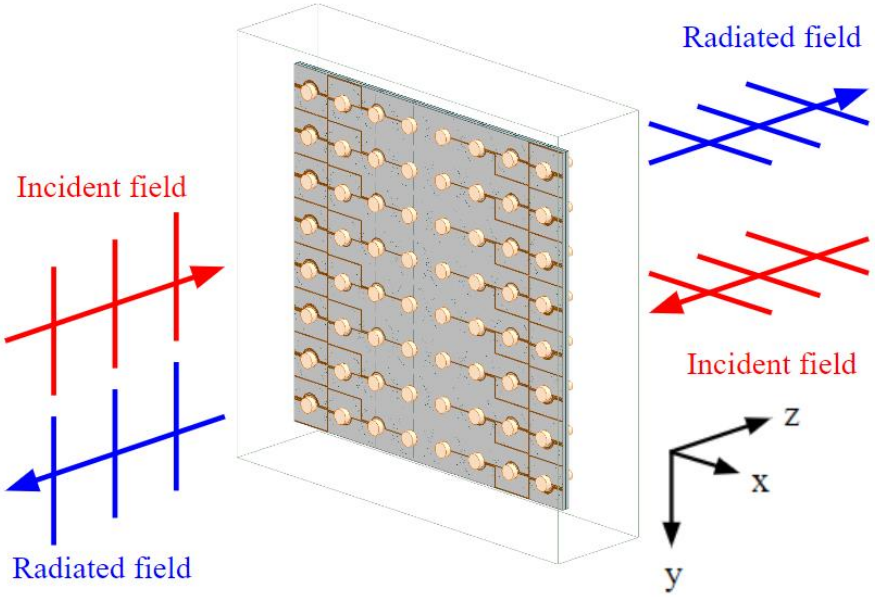

Fig. 3.15. Setup of the scattered fields simulation with an 8×8 RTA.

As the incident plane wave is assigned at different sides of the RTA, the DC bias routing will become receiving side or transmitting side. The results are compared with the RTA without routing. For a good DC bias routing design, the simulation results should be as consistent as possible with the case without routing. Since the simulated structure is a finite-size RTA, the resonant frequencies are not matched the S-parameters of the proposed unit cell. Two frequencies near these modes are selected, which are 11 GHz for lower modes and 12 GHz for higher modes.

doi:10.6342/NTU202302000

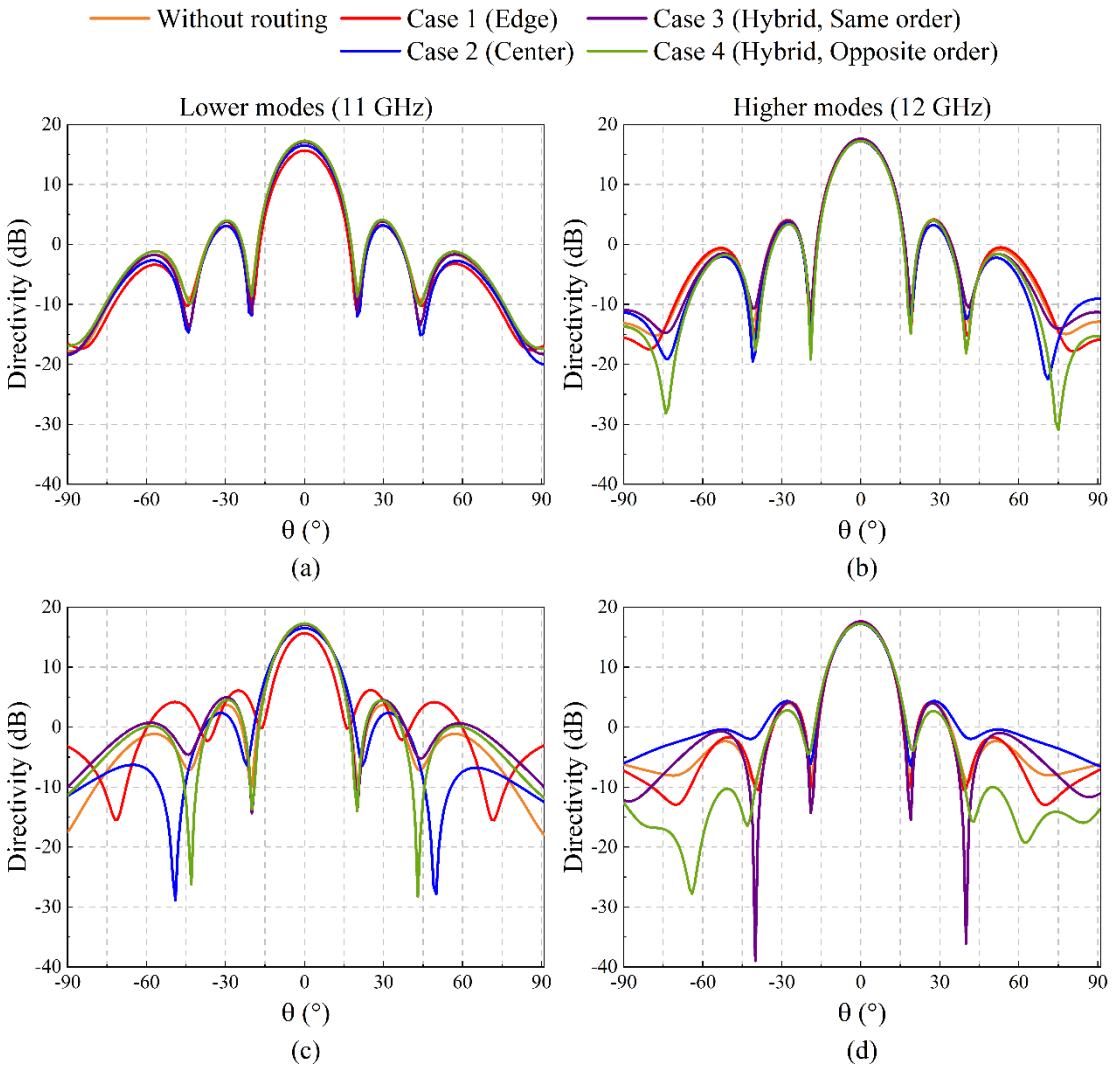

Fig. 3.16. Radiation patterns while the DC bias routing is at the receiving side. (a)(b) On the cut plane perpendicular to the DC bias routing. (c)(d) On the cut plane parallel to the DC bias routing.

First, the DC bias routing is at the receiving side. The radiation patterns on the cut plane perpendicular to DC bias routing are shown in Fig. 3.16 (a)(b). The orange curves are the benchmark. On this cut plane, the variation of the DC bias routing is like a polarizer, so almost all cases fit the benchmark. On the other hand, the radiation patterns on the cut plane parallel to the DC bias routing are drawn in Fig. 3.16 (c)(d). The results imply that Case 1, which is the edge design, has the most impact on the lower modes,

doi:10.6342/NTU202302000

while Case 2, which is the center design, has the most impact on the higher modes. This phenomenon meets the prediction in subsection 3.2.2.

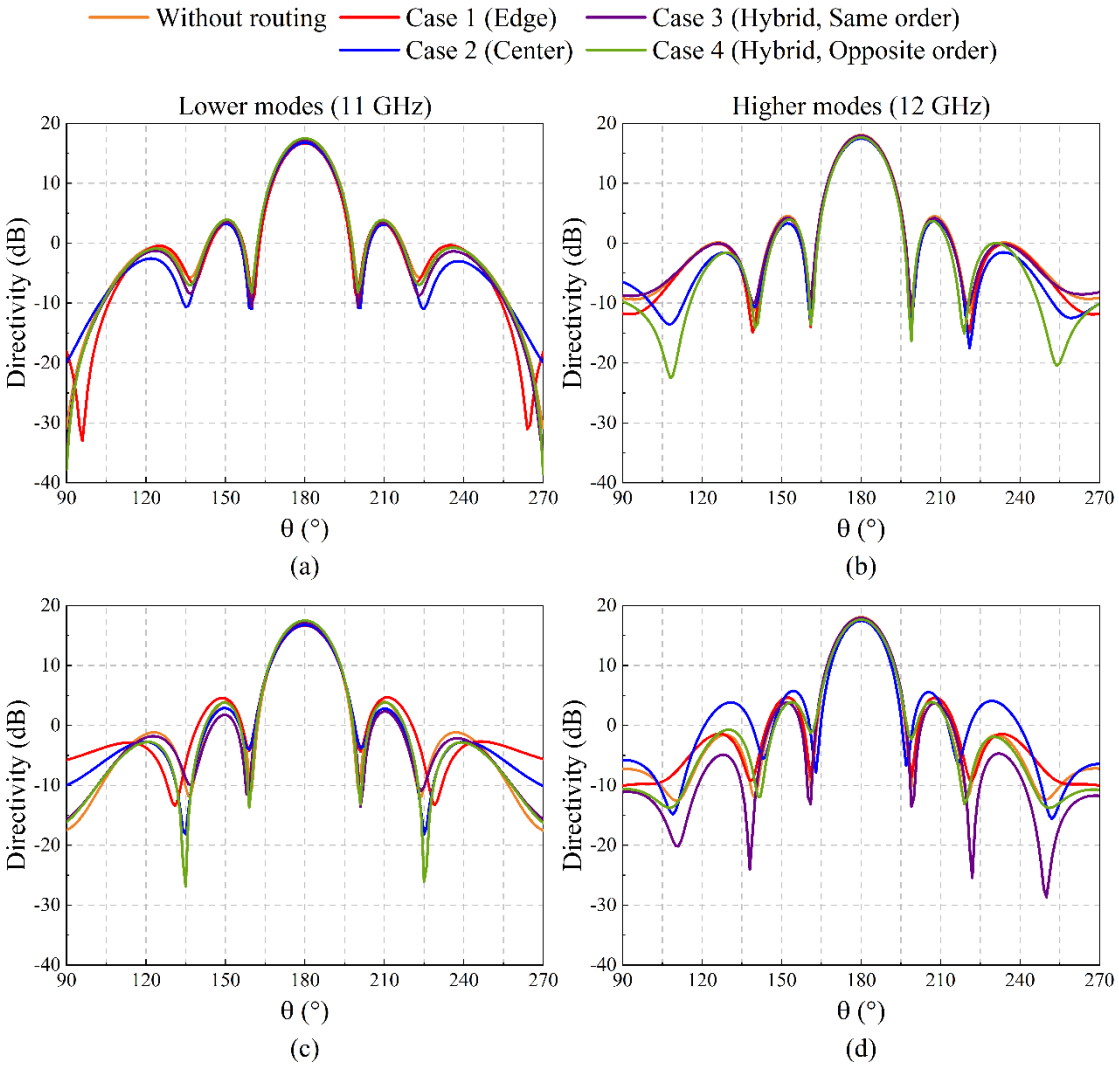

Fig. 3.17. Radiation patterns while the DC bias routing is at the transmitting side. (a)(b) On the cut plane perpendicular to the DC bias routing. (c)(d) On the cut plane parallel to the DC bias routing.

Second, the DC bias routing is at the transmitting side. Similarly, the radiation patterns are shown in Fig. 3.17. The trend is similar to the previous discussion. It is worth noting that for both advanced hybrid designs, the routing impact is relatively small than that of those basic designs. Hence, the advanced hybrid designs perform better and reduce

doi:10.6342/NTU202302000

the routing impact of basic designs.

3.3.2 1-D Subarray Simulation

The aforementioned simulation method is greatly limited by hardware resources, so the length of its DC bias routing is limited to 4 units. It is also known from the results that in the scattered fields simulation, due to the short length, there is little difference between the designs. In [6], [8], and [17], the unit cells in the middle of the RTA and the unit cells on the edge of the RTA are put into PBC for simulation, and roughly estimate the influence of the number of DC bias routing on the RTA. However, the equivalent simulated structure is an infinite RTA, which does not contain the real DC bias routing. Besides, their DC bias routing designs are all simple straight lines. However, the DC bias routing design based on the proposed advanced rule will not be a simple straight line, which is hard to be preliminarily simulated inside the PBC using 1×1 unit cell.

We want to validate the proposed advanced rule in various ways. Therefore, we take advantage of the repeatability of the DC bias routing on the array scale and consider the RTA to be composed of many 1-D subarrays containing the same DC bias routing. In this way, we can reduce the consumption of hardware resources by placing this 1-D subarray in PBC compared with the scattered field simulation, and it can also include a real DC bias routing design. Here, an infinite array composed of such 1-D subarrays is equivalently simulated in PBC, and all elements are excited with the same magnitude. The incident wave is set to be normally incident because the oblique incident wave setting on the PBC of the 1-D subarray is in conflict with the real condition. For a good DC bias routing design, the simulation results obtained from the 1-D subarray simulation will be quite close to the results obtained from the unit cell design, because both of these are infinite arrays composed of the same unit cell, the difference is only the presence or

doi:10.6342/NTU202302000

absence of the DC bias routing. Since the DC bias routing is an additional structure, a good DC bias routing design should make the incident wave feel as invisible as possible.

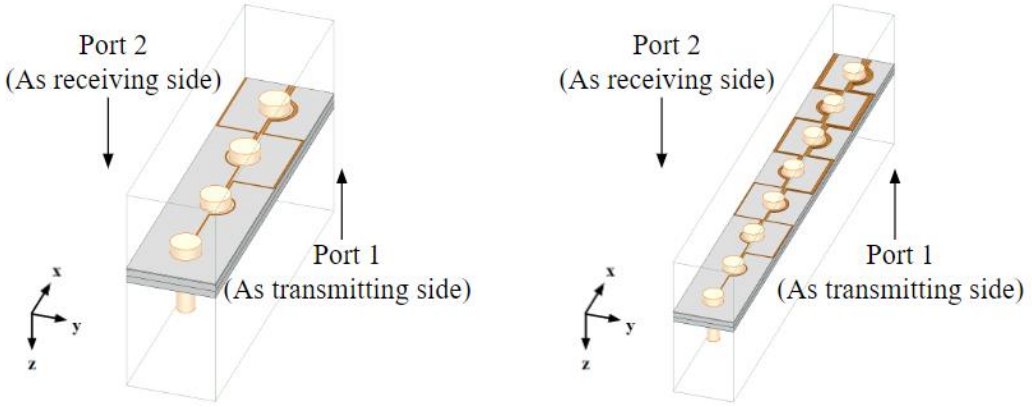

Fig. 3.18. Setup of the 1-D subarray simulation. (a) 1×4 subarray. (b) 1×8 subarray.

The simulation setups are shown in Fig. 3.18. Since the DC bias routing is reduced in half by using both sides of the RTA, the 1×4 subarray is simulated for the 8×8 RTA. Usually, as the RTA becomes larger and larger, the routing impact is also getting serious. Benefiting from the less required computational resources of the 1-D subarray simulation, a larger 1-D subarray can be simulated to estimate the routing impact on a larger RTA. Therefore, the 1×8 subarray is also simulated to estimate the routing impact on the 16×16 RTA, as shown in Fig. 3.18 (b). However, the Floquet ports on the elongated rectangular boundary contain lots of high-order modes. As a preliminary estimation, considering the hardware resources and the computational time, not all higher modes of Floquet ports are included. For the 1×4 subarray, 6 modes are included, while 14 modes are included in the 1×8 subarray. Also, because the actual RTA is not infinite, the simulation results cannot fully represent the real situation. Therefore, there are some numerical errors in the 1-D subarray simulation. Here only the main trend of curves is considered.

doi:10.6342/NTU202302000

Port 1 and Port 2 are set as same as the unit cell simulation in Chapter 2. Here, these ports have additional meanings, which is the DC bias routing being the receiving side or the transmitting side. The simulation results of the 1-D subarray are shown in Fig. 3.19, where the orange curves are the S-parameters of the 1×1 unit cell without routing.

doi:10.6342/NTU202302000

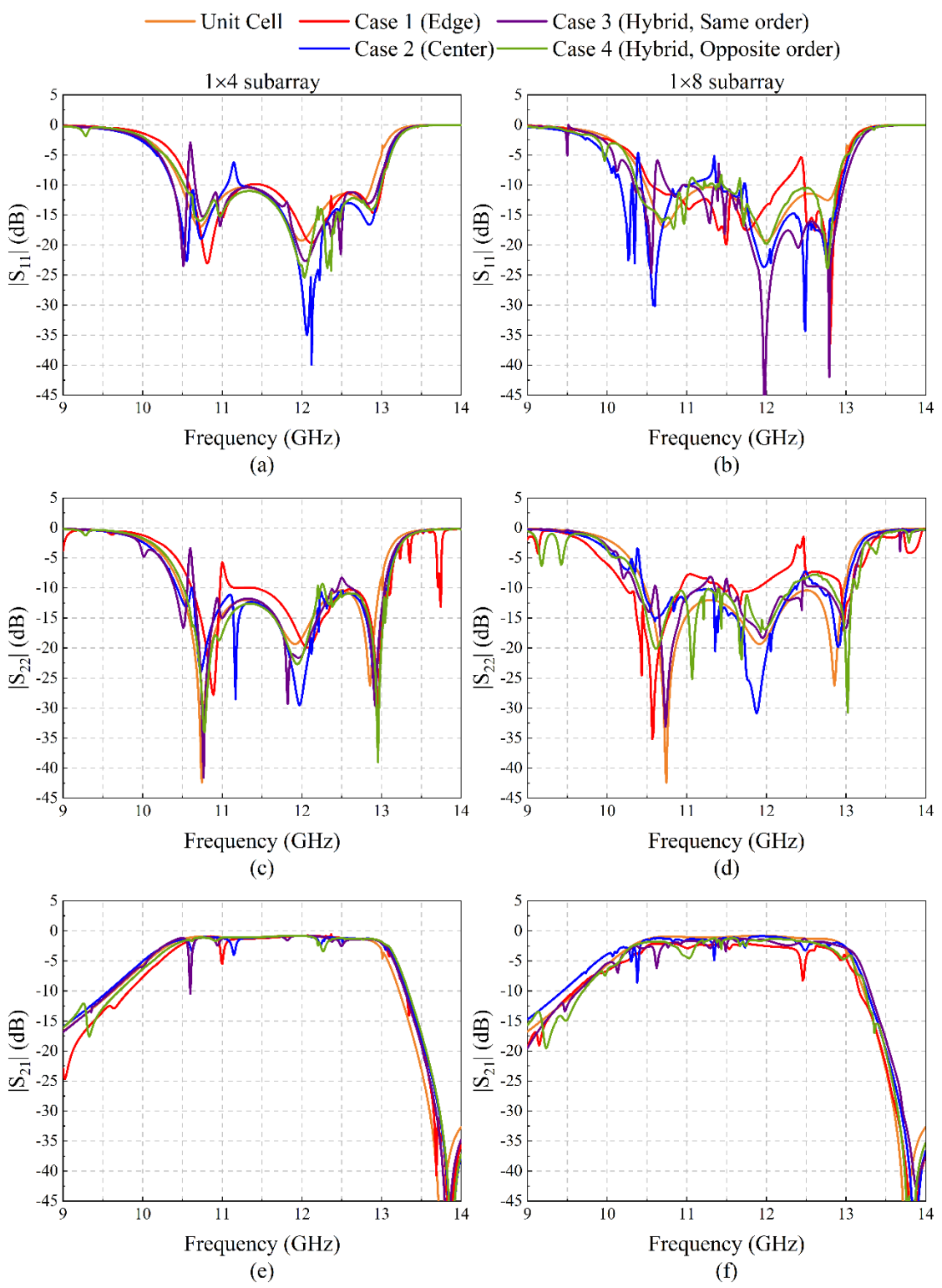

Fig. 3.19. The S-parameters of all DC bias routing cases obtained from the 1-D subarray simulation, where (a)(c)(e) are from the 1×4 subarray and (b)(d)(f) are from the 1×8 subarray.

doi:10.6342/NTU202302000

First, there are many numerical errors in the results of the 1×4 subarray, which implies that the 1-D subarray simulation may have some convergence problems. Based on these results, all cases keep the overall shape of S_{11} and S_{22}, but it is hard to analyze the difference between them resulting from the design way or the numerical errors.

Second, as the size gets larger, the numerical errors greatly increase in the results of the 1×8 subarray. The overall shape of S_{11} and S_{22} are heavily affected. Similarly, it is almost impossible to find the reasons that result in the difference, especially in a longer 1-D subarray. However, with carefully observation, Case 4 is rather stable regardless of the array size among all cases.

In conclusion, although the correctness of the results in the 1-D subarray simulation is still needed to be verified, the advanced rule has a high possibility to improve the DC bias routing design and eliminate the routing impact according to both simulation methods in section 3.3.

doi:10.6342/NTU202302000

Chapter 4 Experimental Setup and Measurement Results

4.1 Enlarged Single Cell Verification Using Waveguide Measurement Technique

4.1.1 Setup of Waveguide Measurement Technique

In [7], [8], [10], and [19], a single unit cell is placed inside waveguides, where waveguides are used to model the PBC. The measured results can be compared with the simulated results of using the PBC in HFSS. The waveguides in use are WR-90 X-band waveguides.

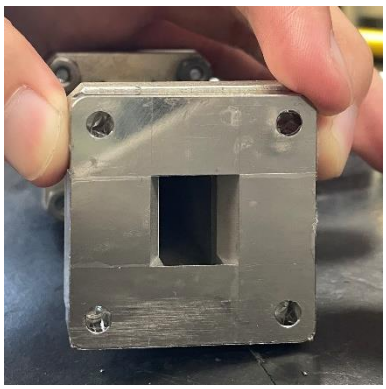

Fig. 4.1. The rectangular-to-square waveguide transition with tape for insulation.

Because the shape of the unit cell is square, a rectangular-to-square, 5-mm thick aluminum waveguide transition is built to transform the aperture. However, the size of the unit cell is too small, causing the cutoff frequency of such a square aperture is higher than the operating band. Thus, the lattice size of the unit cell and the square aperture of the waveguide transition is set to be 15 mm × 15 mm, as shown in Fig. 4.1. The metallic waveguide transition and WR-90 X-band waveguide may cause additional DC leakage,

doi:10.6342/NTU202302000

so tapes are added outside the aperture of waveguide transition for insulation.

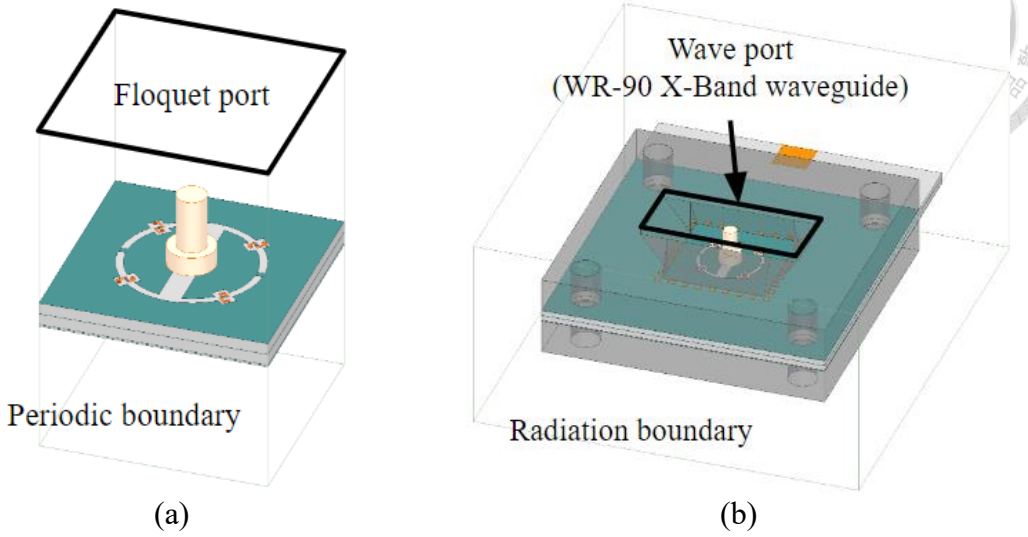

(a) (b)

Fig. 4.2. The simulation setup of (a) the HFSS PBC, and (b) the HFSS WG.

The measured results are compared with two kinds of simulation in HFSS, which are shown in Fig. 4.2. The first one is (a) the enlarged single cell inside the PBC. The second one is (b) the waveguide (WG) simulation which contains the waveguide transitions and uses wave ports. There is a via wall that surrounds outside the aperture to keep the waveguide continuous.

doi:10.6342/NTU202302000

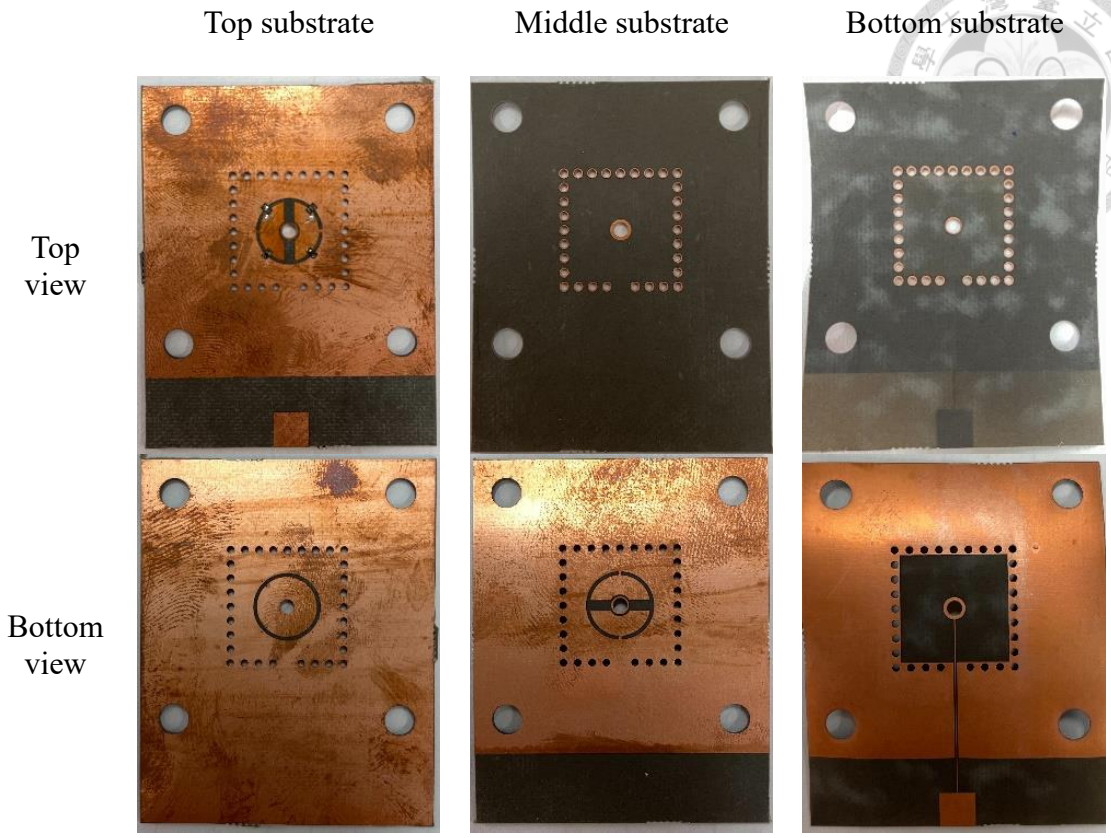

(a)

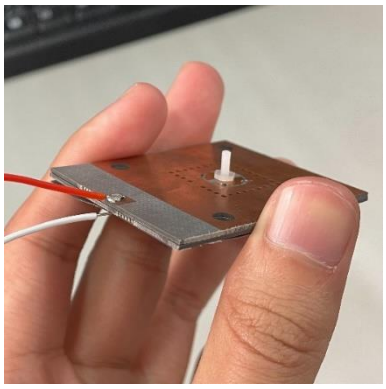

(b)

Fig. 4.3. (a) The top view and bottom view of three substrates of AUT. (b) The combination of three substrates with a plastic screw.

The top view and the bottom view of the enlarged single unit cell prototype are shown in Fig. 4.3 (a). As mentioned in Chapter 2, there are three substrates being fabricated respectively. To control PIN diodes, a simple DC bias line is connected to the center via, which is also the screw hole. The combination of these substrates is shown in

doi:10.6342/NTU202302000

Fig. 4.3 (b).

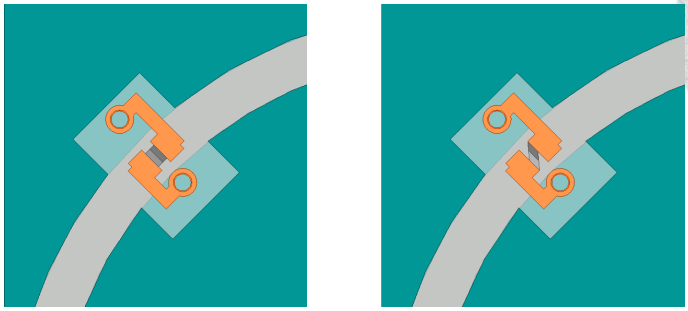

(a) (b)

Fig. 4.4. Connection of PIN diodes (a) in layout and (b) after fabrication.

Before measurement, we observed some fabrication errors. In the unit cell design, the dimension of the pad for PIN diodes soldering was designed as same as the dimension of PIN diodes' mounting pads, which is the ideal case. While drawing the layout, the pad size and location were suggested in the MA4AGP907 datasheet [22]. However, the distance between pads was miscalculated in the Altium component library, which didn't be found before fabrication, as shown in Fig. 4.4 (a). Besides, since the size of PIN diodes is too small, the PIN diodes were placed by hand. Therefore, the bare-copper pads caused the PIN diodes to be rotated counterclockwise. Here, we consider the wrong pad location in the pre-simulation and suppose all PIN diodes are rotated 45° in the post-simulation, as shown in Fig. 4.4 (b). Although the S-parameters will be affected, the measurement can still help us to verify the correctness of the simulation.

doi:10.6342/NTU202302000

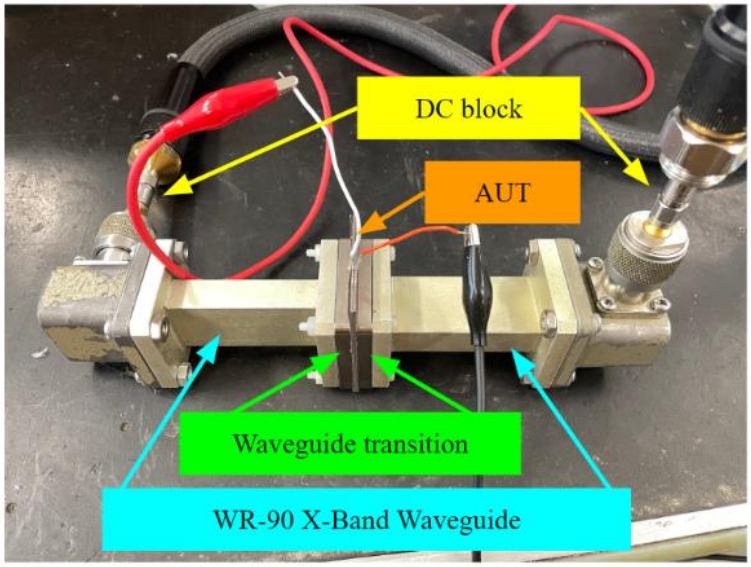

Fig. 4.5. The measurement setup of the waveguide measurement technique.

The measurement setup is shown in Fig. 4.5. Since the measurement includes the DC bias, the DC blocks are added to protect the VNA. The two waveguides are placed orthogonally to measure the correct polarization of the unit cell. The opposite polarity of the DC bias is given to generate two phase shifts of the 1-bit phase quantization.

4.1.2 Measurement Results

The measured frequency range is from 9.25 GHz to 11.25 GHz for two reasons. First, the operating frequency of the WR-90 X-band waveguide is from 8.2 GHz to 12.4 GHz. Second, the resonant frequency of the enlarged single cell is not as wideband as before, so we measure the first resonant mode only. But the setting in HFSS is up to 12.4 GHz in the both simulations.

doi:10.6342/NTU202302000

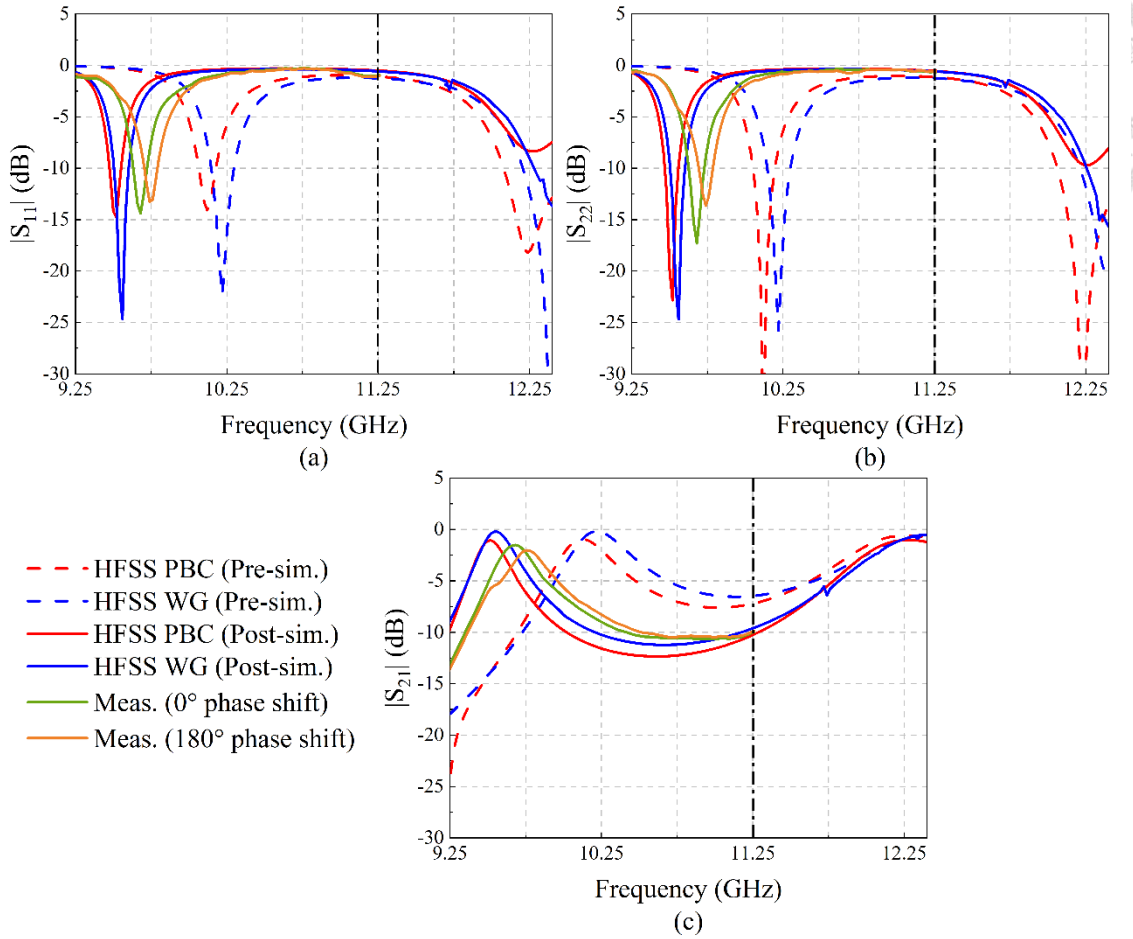

Fig. 4.6. The simulated and measured (a) S_{11}, (b) S_{22} and (c) S_{21}.

The S-parameters are shown in Fig. 4.6. The green curves and the orange curves represent the 0° phase shift unit cell and the 180° phase shift unit cell, respectively. The red curves and the blue curves represent the HFSS PBC simulation and the HFSS WG simulation. The S-parameters of the enlarged single cell are deteriorated, but there are still multiple resonant modes. The post-simulated results are more fitting to the measured results. The curves of both phase shifts unit cells are close to each other and have the same trend as the HFSS PBC simulation and HFSS WG simulation.

doi:10.6342/NTU202302000

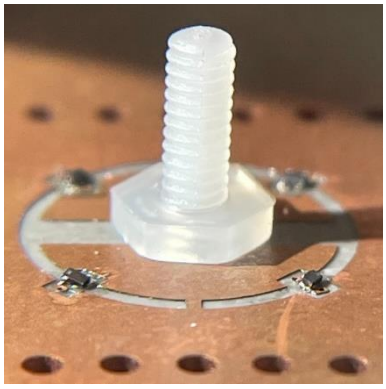

Fig. 4.7. A closer look of PIN diodes soldering.

There is still a frequency mismatch. As shown in Fig. 4.7, the hand-placed PIN diodes have different amounts of tin and different tilt angles. These factors are hard to be modeled in the post-simulation. It should be the reason why the post-simulated results didn't perfectly match the measured results, and why the results of 1-bit unit cell pairs have slight differences.

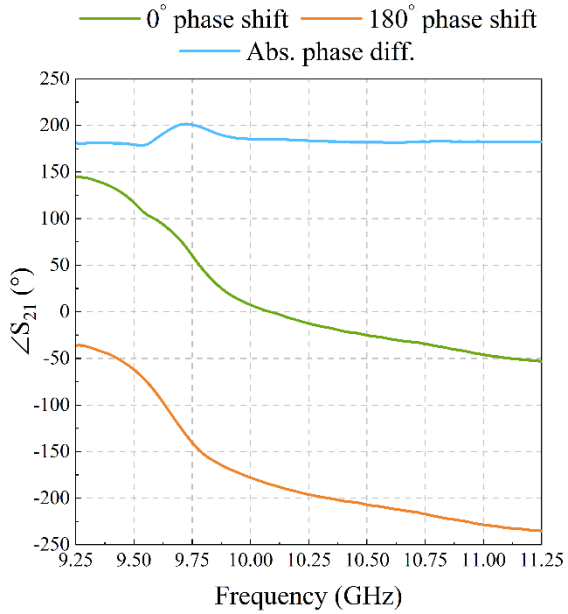

Fig. 4.8. The measured transmission phase of the 1-bit unit cell pairs.

doi:10.6342/NTU202302000

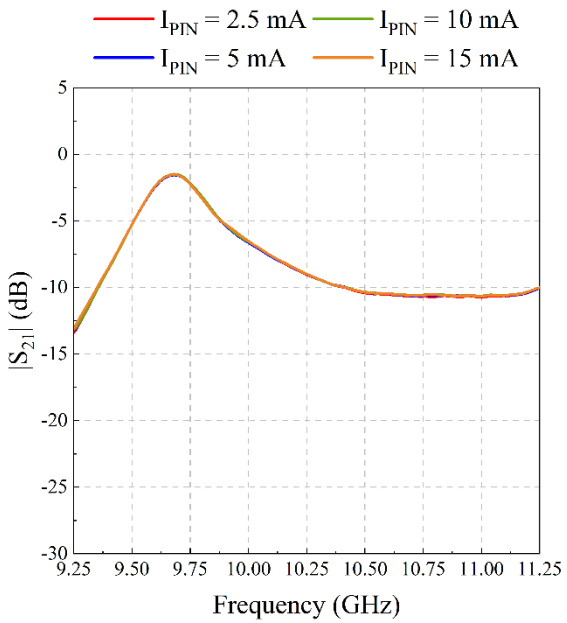

Fig. 4.9. The S_{21} of the 0° phase shift unit cell under different PIN diode current (I_{PIN}).

On the other hand, the phase difference of the 1-bit unit cell pairs is shown in Fig. 4.8. It keeps near 180° in the entire frequency range. Moreover, the measured S_{21} of different current values that flow across PIN diodes (I_{PIN}) is shown in Fig. 4.9. It reveals that for our proposed unit cell, the current value when PIN diodes are turned on will not affect the RF transmission performance. The result verifies the reconfigurability of the proposed unit cell and the RLC model of PIN diodes in HFSS. In conclusion, excludes the complicated effect due to mounting by hand, the measured results fit the simulated results, and the proposed 1-bit unit cell pairs have similar transmission characteristics and 180° phase difference controlled by opposite DC bias polarity.

doi:10.6342/NTU202302000

4.2 Beam Steering Experiment at 11.5 GHz

4.2.1 Setup of the Prototype RTA with Microcontroller (MCU)

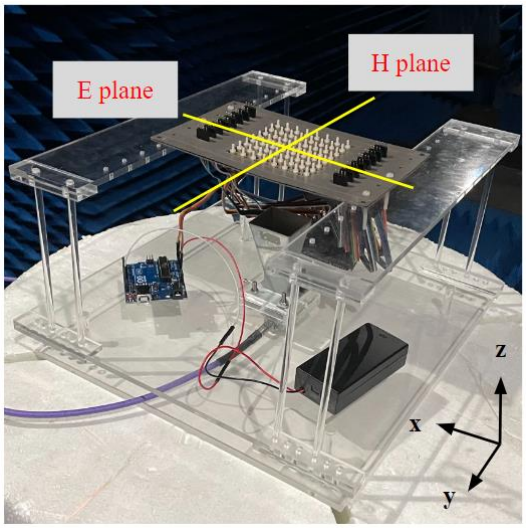

Fig. 4.10. The setup of the beam steering measurement.

An RTA based on the proposed unit cell and the DC bias routing design is fabricated to verify the beam-steering capability. The measurement setup is shown in Fig. 4.10. The measurement has been established in the anechoic chamber and performed at the center frequency, which is 11.5 GHz. There are three components in the setup, the RTA based on the proposed unit cell and the DC bias routing design, the phase control circuit, and the holder with the feed source.

doi:10.6342/NTU202302000

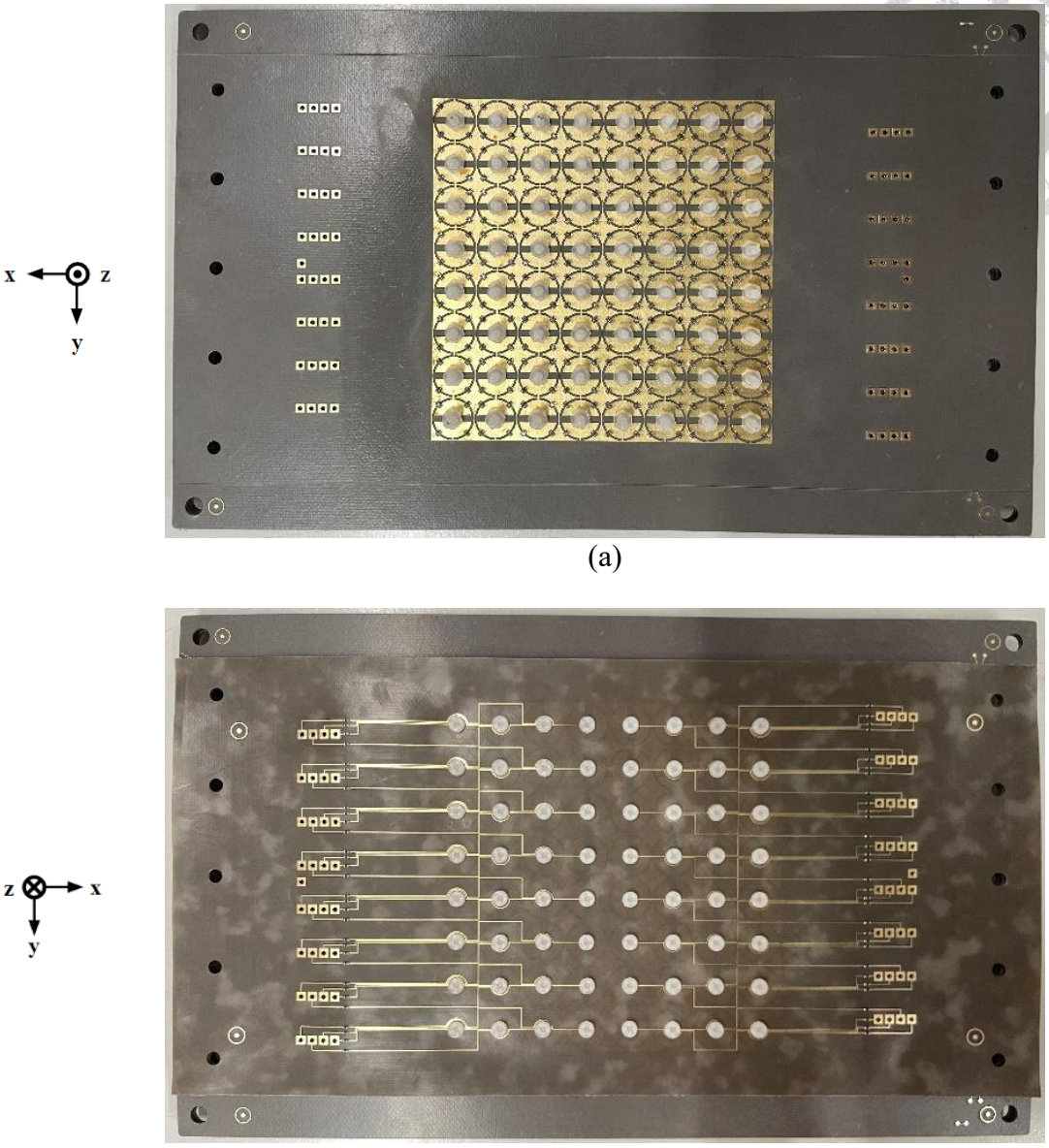

Fig. 4.11. The (a) top view and the (b) bottom view of the 8×8 RTA.

First is the RTA based on the proposed unit cell and the DC bias routing design. Limited by the fabrication cost, an 8×8 size is chosen as a small prototype, which is also for simulation convenience as discussed in subsection 3.3.1. Therefore, the fabricated RTA in this section is used only for the validation of beam-steering capability. A total of 256 PIN diodes and 64 plastic screws are used, as shown in Fig. 4.11 (a). At this time, we have fixed the pad location problem in subsection 4.1.1, but the PIN diodes were still

doi:10.6342/NTU202302000

placed by hand. At the middle layer, two GND pins are added to provide the DC ground in case. The PCB size is larger than the RTA to leave space for DC pins. In section 3.2, four DC bias routing designs are proposed in which Case 3 and Case 4 are based on our advanced DC bias routing rule. Here, we fabricate Case 4 based on its good simulated results in section 3.3. Outside the RTA, the DC bias routing is extended as a straight line, which follows the basic DC bias routing rules. At the end of each DC bias routing path, a total of 64 current-limiting resistors are added because the DC source is provided by MCU, where the total current is limited. Also, 64 DC pins are added for the wire connection, as shown in Fig. 4.11 (b).

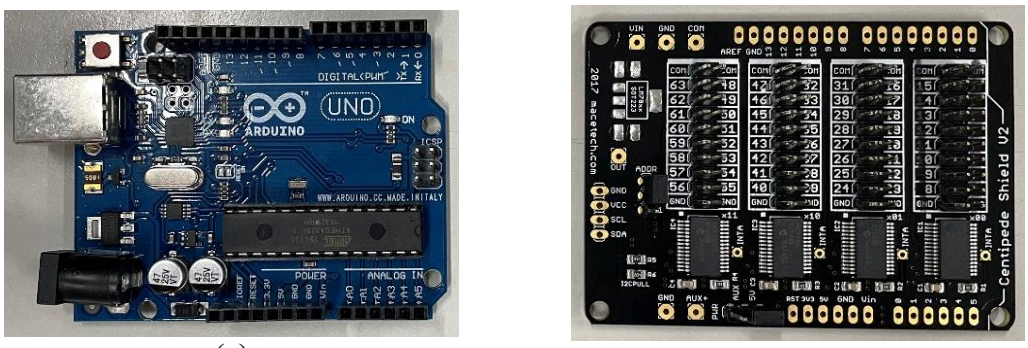

(a) (b)

Fig. 4.12. Components of the phase control circuit. (a) Arduino Uno. (b) Centipede shield V2.

The second part is the phase control circuit, as shown in Fig. 4.12. To control the small prototype 8×8 RTA, an Arduino Uno is chosen to be the MCU. However, the I/O ports are not enough to control all unit cells. Therefore, a Centipede shield V2 [23] is added to provide additional 64 I/O ports. These ports are connected with the RTA through Dupont wires. To control the DC bias of each unit cell, the MCU should provide a positive bias and a negative bias with respect to the GND pin. But the Arduino Uno can only control its output pins to be 5 V (HIGH) or 0 V (LOW).

doi:10.6342/NTU202302000

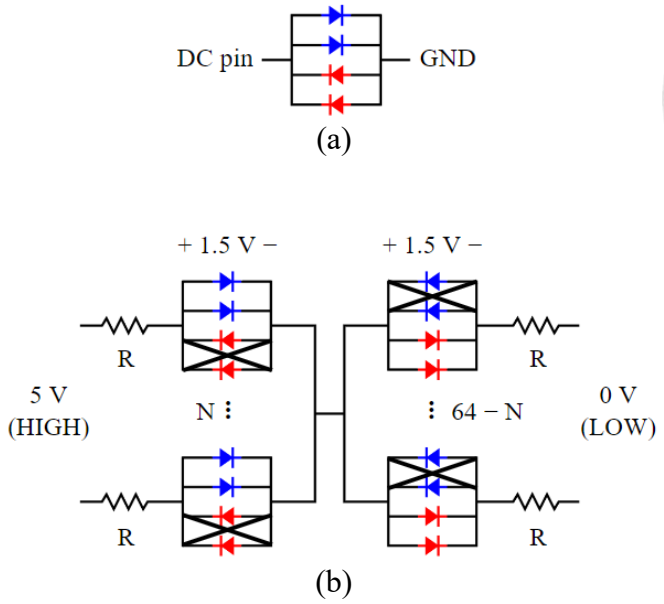

Fig. 4.13. The DC equivalent circuit model of (a) the proposed unit cell and (b) the 8×8 RTA.

The DC equivalent circuit model of the proposed unit cell is shown in Fig. 4.13 (a). Referring to Fig. 2.3 (c), two PIN diode pairs are placed in opposite orientations. When the DC pin gets a positive bias, the blue pair will be turned ON and the red pair will be turned OFF at the same time. Similarly, when the DC pin gets a negative bias, the blue pair will be turned OFF and the red pair will be turned ON at the same time. The equivalent circuit of the 8×8 RTA is shown in Fig. 4.13 (b). The unit cells in the same group are shunted together and all unit cells are connected to the same GND. When blue PIN diode pairs are turned ON, it will force the voltage across to be near 1.5 V, then the voltage across all red PIN diode pairs is still positive. Thus, unless all unit cells are assigned to have the same phase shift, the GND can be floated, then the MCU is used to assign each unit cell to be in the HIGH group or in the LOW group.

$$I_{Total} = N \cdot I_{HIGH} = (64 - N) \cdot I_{LOW} \tag{4.1}$$

$$(I_{HIGH} + I_{LOW}) \cdot R = (5 - 2 \cdot 1.5)\ V \tag{4.2}$$

doi:10.6342/NTU202302000

To determine the resistance of the limiting current resistors, suppose there are N unit cells in the HIGH group and 64 – N unit cells in the LOW group, the KCL and the KVL are as (4.1) and (4.2). The current flowing into the unit cell in the HIGH group (I_{HIGH}) and the current flowing into the unit cell in the LOW group (I_{LOW}) can be solved as (4.3).

$$\begin{cases} I_{HIGH} = \dfrac{64 - N}{32R} = 2 \cdot I_{PIN,HIGH} \\ I_{LOW} = \dfrac{N}{32R} = 2 \cdot I_{PIN,LOW} \end{cases} \tag{4.3}$$

When performing beam steering, the number of unit cells in the HIGH group and LOW group are different, which makes $I_{PIN,\,HIGH} \neq I_{PIN,\,LOW}$. In subsection 4.1.2, the measured results reveal that the current value of PIN diodes doesn't influence the RF transmission performance. Therefore, considering the power capability of the MCU, we choose the resistance R to be 25 Ω, which limits the current to under 20 mA. In addition, two 4.2 V batteries are series to provide the DC power.

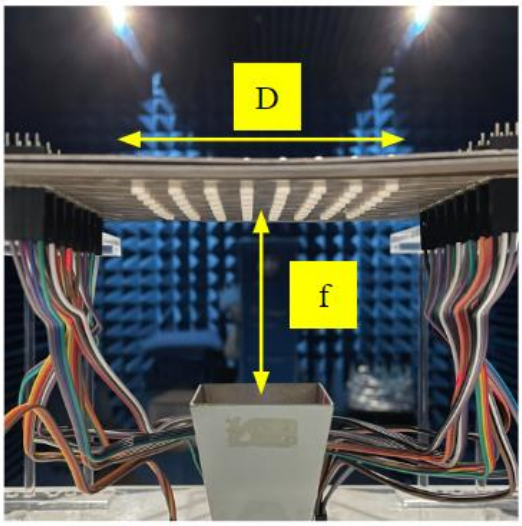

Fig. 4.14. The focal length and the diameter of the RTA.

The last part is the holder with a feed source. The holder is made of acrylic board. The feed source is a pyramidal X-band horn antenna (Ainfoinc LB-90-10-A [24]), whose

doi:10.6342/NTU202302000

beam pattern can be modeled as $\cos^q(\theta)$ with q = 10. The RTA size D is equal to 76.8 mm, which is limited by the fabrication cost. The f is chosen to make sure the receiving power from the horn antenna at the edge of the RTA is -10 dB, thus the f/D ratio is 0.755, as shown in Fig. 4.14. The oblique incident angle is around 33.5° at the edge of the RTA.

4.2.2 Phase Distribution Optimization

At such a distance, the incident wave will be a spherical wave but not a plane wave. The phase distribution for beam steering is needed. The quantized phase distribution is calculated by (1.1) and (1.2). In [13], an optimized phase distribution for the broadside main beam can be calculated. Besides, the optimized broadside phase distributions in the entire operating band are all the same because the prototype RTA is too small to provide enough phase variation.

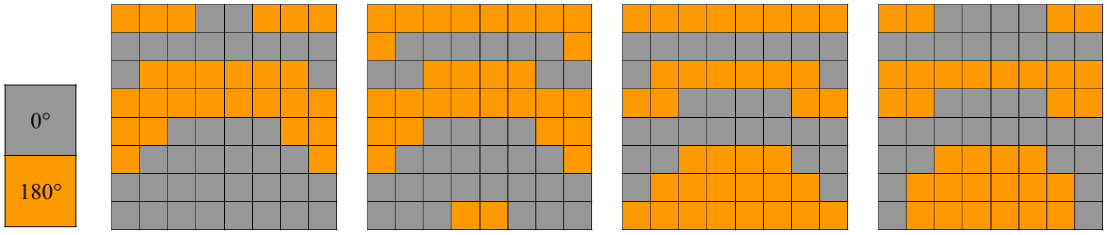

Fig. 4.15. The optimized phase distribution of the 8×8 RTA for θ = (a) 30°, (b) 40°, and (c) 50°, and (d) the non-optimized phase distribution of the 8×8 RTA for θ = 40°.

As for the phase distribution optimization in each steering angle, the formula in [13] is no more applicable in our small prototype RTA. For example, the optimized phase distribution for 40° will cause the main beam point to 30°, while the optimized phase distribution for 50° will make the main beam point to 40°. As shown in Fig. 4.15, the optimized phase distribution for 50° is quite similar to the non-optimized phase distribution for 40°, which has much phase variation compared with the optimized one.

doi:10.6342/NTU202302000

4.2.3 Measurement Results in Anechoic Chamber

After the phase distribution optimization, the feasibility of the beam steering and the correctness of the simulation are validated in this subsection. Here, we didn't compare the difference between all DC bias routing cases in the simulation. The reason is that the routing impact is affected by the array size. Due to the small size of the 8×8 RTA, the distance between the RTA and the horn antenna is only $2.23\lambda_c$, so the coupling between the horn antenna and the DC bias routing cannot be ignored. Therefore, it is hard to analyze and extract the routing impact caused by different designs in this small prototype RTA measurement.

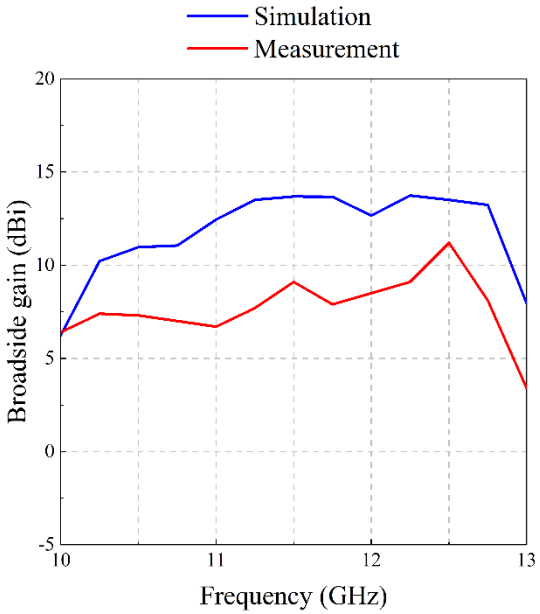

Fig. 4.16. The broadside gain plot of the 8×8 RTA.

The simulated and measured broadside gain are shown in Fig. 4.16. The measured broadside gain is 9.1 dBi at 11.5 GHz, with the 3-dB gain bandwidth of 25% and the related aperture efficiency of 7.5%. On the other hand, the radiation patterns of different beam steering angles at both principal planes at 11.5 GHz are shown from Fig. 4.17 to

doi:10.6342/NTU202302000

Fig. 4.21. The steering angle is from θ = 0° to 40°, which is limited by the array size and the resolution of quantized phase distribution. Also, the sidelobe levels of all steering angles at both principal planes are summarized in Table 4.1.

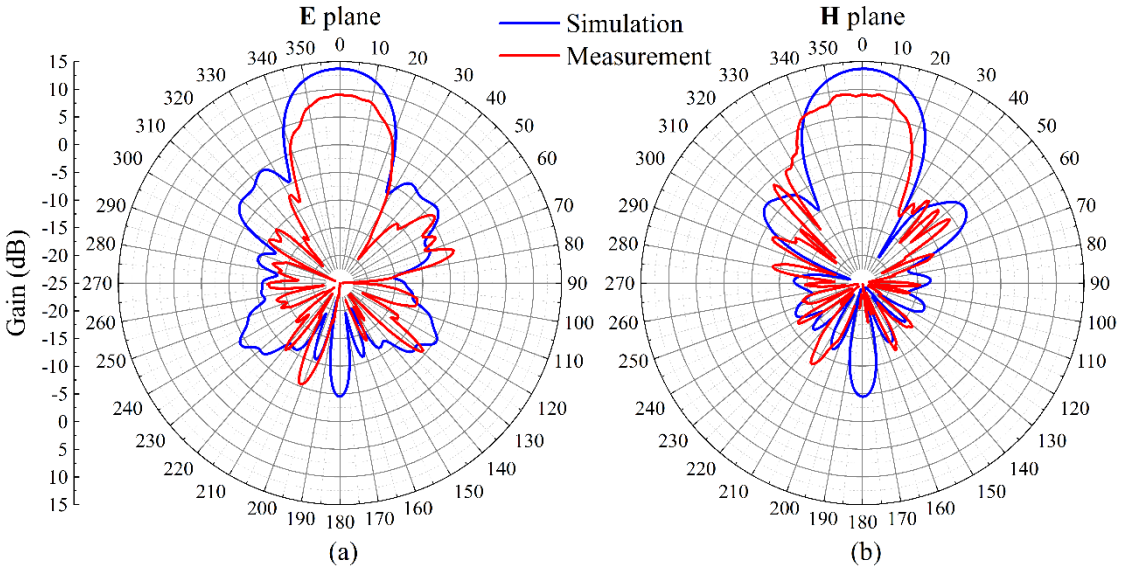

Fig. 4.17. Radiation pattern of the 8×8 RTA with steering angle θ = 0° at (a) the E plane and at (b) the H plane.

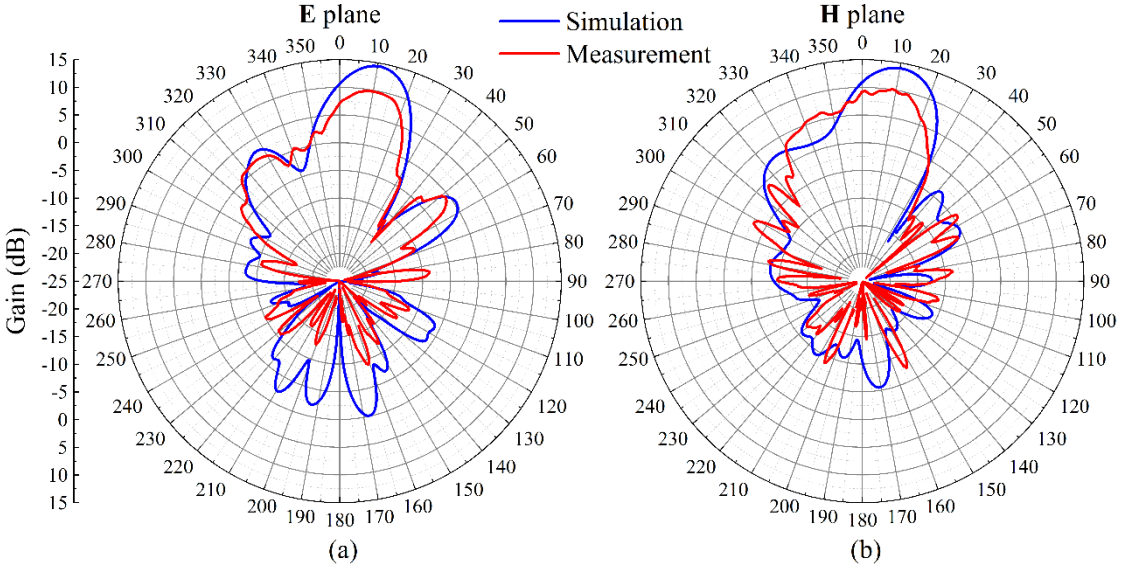

Fig. 4.18. Radiation pattern of the 8×8 RTA with steering angle θ = 10° at (a) the E plane and at (b) the H plane.

doi:10.6342/NTU202302000

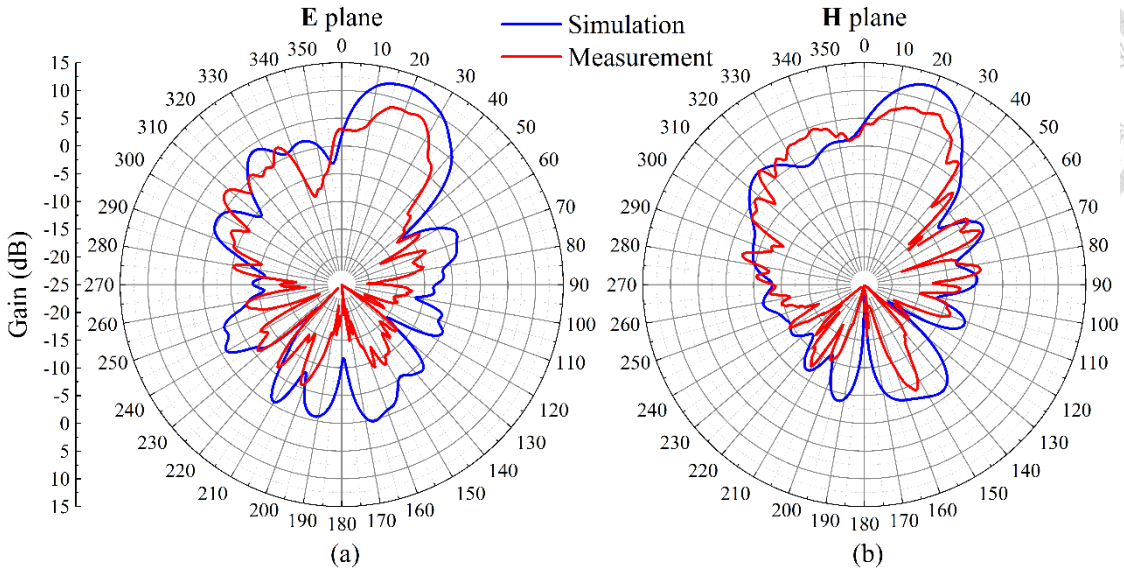

Fig. 4.19. Radiation pattern of the 8×8 RTA with steering angle θ = 20° at (a) the E plane and at (b) the H plane.

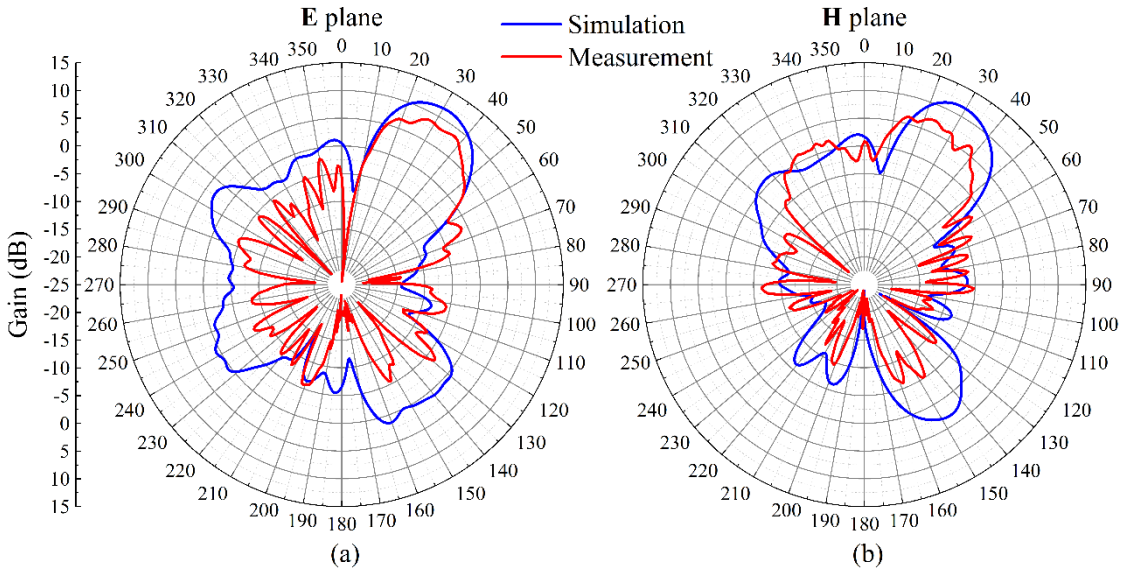

Fig. 4.20. Radiation pattern of the 8×8 RTA with steering angle θ = 30° at (a) the E plane and at (b) the H plane.

doi:10.6342/NTU202302000

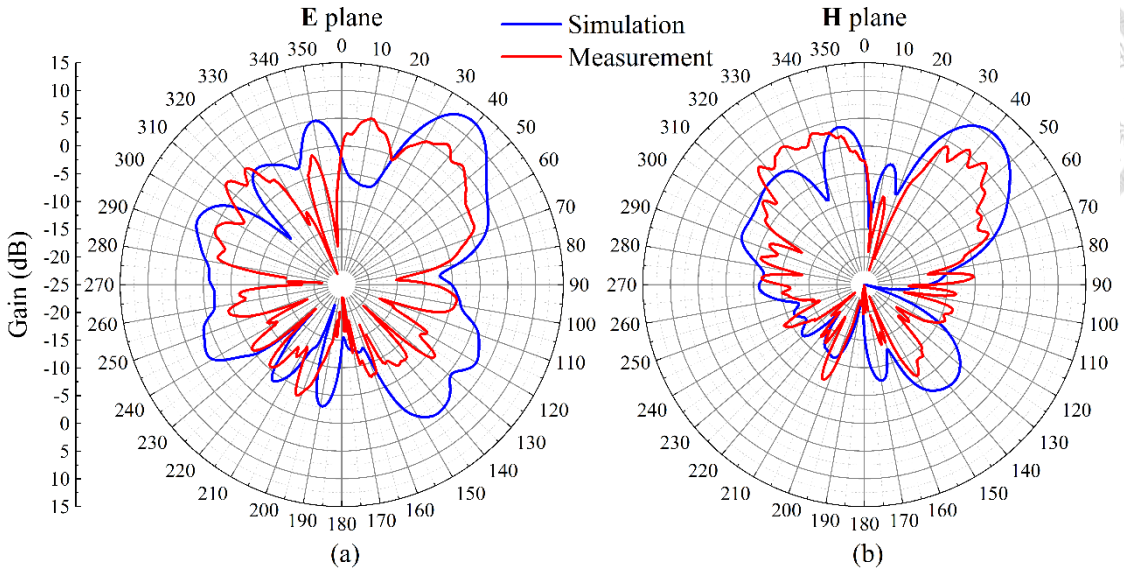

Fig. 4.21. Radiation pattern of the 8×8 RTA with steering angle θ = 40° at (a) the E plane and at (b) the H plane.

Table 4.1. The sidelobe levels of all steering angles at both principal planes.

Steering angle θ	0°	10°	20°	30°	40°
SLL at E plane (dB)	13.2	11.9	7.6	9.5	1.2
SLL at H plane (dB)	15.1	3.6	3.7	4.8	2.2

The measured maximum steering gain losses of the E plane and H plane are 2.3 dB and 3.3 dB, respectively. It is apparent that the measured peak gain and the simulated peak gain have at least a 5 dB difference within the operating band and even in every steering angle. Also, the measured radiation patterns do not exactly align with the simulated radiation patterns where the error is more severe at a large steering angle. The following are the possible reasons.

First, as discussed in section 2.4, the oblique incidence will increase the insertion loss near 11.5 GHz. Not all unit cells on the RTA has a large oblique incident angle, therefore, the average insertion loss is approximately 0.5 dB.

Second, as mentioned in subsection 4.2.1, the PIN diodes were still placed by hand.

doi:10.6342/NTU202302000

Each PIN diode has its unique tilt angle. Similar to the post-simulation in subsection 4.1.1, a unit cell with all PIN diodes rotated 45° is simulated. As shown in Fig. 4.22, the insertion loss at 11.5 GHz increases by near 2.3 dB.

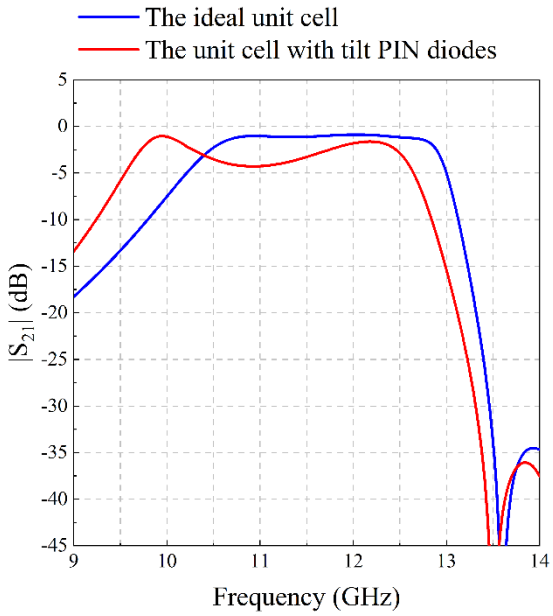

Fig. 4.22. The S_{21} of unit cells in the post simulation.

Third, some unit cells are “dead” either due to soldering failure of PIN diodes or PIN diodes damage when assembling three substrates using screws. It is hard to check which PIN diode is broken because all PIN diodes are shunt pairs by pairs. The confirmed broken PIN diode pairs are shown in Fig. 4.23. Although these unit cells are actually “half-dead”, the phase quantization error can be minimized by carefully assigning the phase distribution.

doi:10.6342/NTU202302000

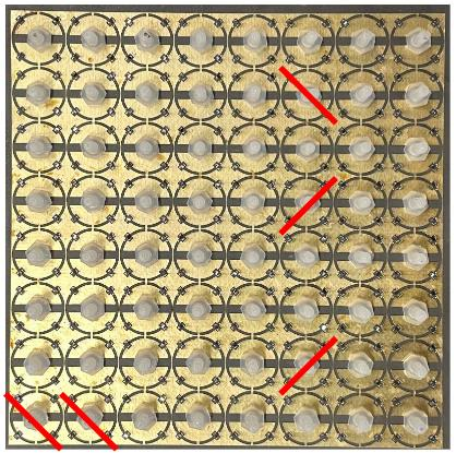

Fig. 4.23. The confirmed broken PIN diode pairs marked by red lines on the 8×8 RTA.

The last error factor is the additional structures, such as the acrylic holder and the Dupont wires around the RTA and the feed source. These additional structures are not included in the simulation. Besides, lots of ripples exist in the measured radiation pattern indicate that the additional structures need to be considered as part of the antenna aperture, especially when the main beam steers to a larger angle. All the error factors are summarized in Table 4.2.

Table 4.2. Gain loss factors analysis.

Loss factors analysis	**Approximate loss (dB)**
Oblique incidence error	0.5
Fabrication error	2.3
Distribution error	1
Additional structures	0.5

4.2.4 Comparison with Other Works

Table 4.3 compares the important parameters of the RTA with other related works. As a small prototype RTA, whose f/D ratio is not optimized, its gain and aperture efficiency are worse than all other works. Also, the measured I_{PIN} is near 5 mA, which is limited by the current-limiting resistors, the Arduino Uno, and the Centipede shield. Thus

doi:10.6342/NTU202302000

the total DC power consumption of the RTA itself is approximate 0.96 W.

On the other hand, the 3-dB gain bandwidth achieves 25% and the steering loss is less than 3.3 dB. The wideband characteristic of the proposed unit cell is verified by the small prototype RTA. The bandwidth is better than most of works except of [18]. The reason is that [18] is twice as thick as our work and is designed at lower frequency. Although there are some fabrication consideration that degrade the results and limit the performance, the reconfigurability of the wideband 8×8 prototype RTA is verified and the steering angle is up to 40° at both principal planes.

Table 4.3. Comparison with other RTAs.

Ref.	Freq. (GHz)	3-D size in λ_c	DC power (W)	Gain (dBi)	e_a (%)	3-dB (1-dB) gain BW (%)	Steering angle/loss E (dB) × H (dB)
[6]	12.8	5.2×5.2×0.14	N/A	18.4	20.2	9.4 (N/A)	50° (4.2) × 40° (3.4)
[11]	10	10×10×0.1	4.8	22.7	16	15.8 (N/A)	40° (2.8) × 70° (7.6)
[12]	12.2	8×8×0.19	N/A	22.1	21.2	12.3 (N/A)	60° (4.8) × 60° (3.3)
[17]	10	5×5×0.14	1.4	19.1	25.8	15.9 (N/A)	50° (2.8) × 50° (3.4)
[18]	5	4.7×4.7×0.16	N/A	16.8	18.4	45 (17)	40° (2.3) × 40° (2.3)
This work	**11.5**	**2.9×2.9×0.07**	**0.96**	**9.1**	**7.5**	**25 (14.7)**	**40° (2.3) × 40° (3.3)**

doi:10.6342/NTU202302000

Chapter 5 Conclusion and Future Work

5.1 Conclusion

In this thesis, a wideband 1-bit reconfigurable unit cell for beam-steering transmitarray is proposed. Four PIN diodes are added and can be controlled by using only one DC bias line. The proposed unit cell generates opposite polarization by performing polarization rotation without using any polarizer layers and air layers. The simple structure is easy to be fabricated and has a wide operating band at the same time. The reconfigurability of the proposed unit cell has been verified by using the waveguide measurement technique. The 3-dB insertion loss bandwidth is 23.8% and the minimum insertion loss is 0.798 dB.

Besides, four designs of the DC bias routing without using RF chokes are proposed according to the routing analysis. Case 1 and Case 2 are based on the basic DC bias routing rules, while Case 3 and Case 4 are based on the proposed advanced DC bias routing rule. That is, the DC bias routing design of a wideband, multi-modes FSS-based unit cell without polarizer layers should minimize and fragment the mode destruction area of different modes. In addition, two simulation methods for estimating the impact of the DC bias routing are proposed in this work.

Limited by the fabrication cost, a prototype 8×8 RTA consisting of the proposed unit cell and the DC bias routing design is fabricated and tested. The measured broadside gain is 9.1 dBi and the related aperture efficiency is 7.5%. The analysis of gain loss factors has been done. The RTA has a 3-dB gain bandwidth of 25% and achieves a beam steering angular range of 40° with a steering loss of less than 3.3 dB at both principal planes.

doi:10.6342/NTU202302000

5.2 Future work

In Chapter 2, the proposed unit cell needs a plastic screw to fix three substrates, which made it difficult to assemble a large RTA. On the other hand, PIN diodes were placed by hand, which caused PIN diodes to be sometimes flaked during combination. Also, only a small prototype RTA using less than 100 elements is fabricated in this work, whose performance is not good enough due to its limited size. The fabrication cost of components in the RTA is listed in Table 5.1. In the future, we will keep finding a suitable manufactory to make our unit cell much robust and fabricate a larger RTA in a low-cost way for beam-steering applications.

Table 5.1. The fabrication cost of components in the RTA.

Components in the 8×8 RTA	**Cost (NTD)**
PCB fabrication	75000
PIN diodes	53000
Acrylic holder	3000
Phase control circuit	1000
Total	132000

On the other hand, in section 3.3, the preliminary simulation methods for estimating the routing impact are assuming that the incident wave is a uniform plane wave so that we can compare the difference only caused by routing designs. These methods are suitable for a large-size RTA. As for a small-size RTA, there are a lot of factors to consider, such as phase distribution, spherical incident wave, and coupling with the feed source. In the future, we will keep studying to find a simple way to estimate the routing impact for small-size RTA despite that it is quite time-consuming and corresponds to a very complicated mechanism.

doi:10.6342/NTU202302000

References

[1] Ahmed H. Abdelrahman; Fan Yang; Atef Z. Elsherbeni; Payam Nayeri; Constantine A. Balanis, *Analysis and Design of Transmitarray Antennas*, Morgan & Claypool, 2017.

[2] A. Munoz-Acevedo, P. Padilla and M. Sierra-Castaner, "Ku band active transmitarray based on microwave phase shifters," 2009 3rd European Conference on Antennas and Propagation, 2009, pp. 1201-1205.

[3] C. Tian, Y. Jiao and G. Zhao, "Circularly Polarized Transmitarray Antenna Using Low-Profile Dual-Linearly Polarized Elements," in *IEEE Antennas and Wireless Propagation Letters*, vol. 16, pp. 465-468, 2017.

[4] L.-Z. Song, P.-Y. Qin and Y. J. Guo, "A High-Efficiency Conformal Transmitarray Antenna Employing Dual-Layer Ultrathin Huygens Element," *IEEE Transactions on Antennas and Propagation*, vol. 69, no. 2, pp. 848-858, Feb. 2021.

[5] Y.-L. Li, S.-W. Wu, and S.-Y. Chen, "Simplified Transmitarray Unit Cell for 1-Bit Beam-Steering Operation," IEEE AP-S International Symposium and URSI Radio Science Meeting, Montreal, Quebec, Canada, Jul. 2020.

[6] X. Wang, P.-Y. Qin, A. T. Le, H. Zhang, R. Jin and Y. Jay Guo, "Beam Scanning Transmitarray Employing Reconfigurable Dual-Layer Huygens Element," in *IEEE Transactions on Antennas and Propagation*.

[7] B. D. Nguyen and C. Pichot, "Unit-Cell Loaded With PIN Diodes for 1-Bit Linearly Polarized Reconfigurable Transmitarrays," in *IEEE Antennas and Wireless Propagation Letters*, vol. 18, no. 1, pp. 98-102, Jan. 2019.

[8] W. Pan, C. Huang, X. Ma, B. Jiang, and X. Luo, "A dual linearly polarized transmitarray element with 1-bit phase resolution in X-band," *IEEE Antennas Wireless Propag. Lett.*, vol. 14, pp. 167–169, 2015.

[9] B. Rana, I.-G. Lee and I.-P. Hong, "Digitally Reconfigurable Transmitarray With Beam-Steering and Polarization Switching Capabilities," in *IEEE Access*, vol. 9, pp. 144140-144148, 2021.

[10] L. Di Palma, A. Clemente, L. Dussopt, R. Sauleau, P. Potier, and P. Pouliguen, "1-bit reconfigurable unit cell for Ka-band transmitarrays," *IEEE Antennas Wireless Propag. Lett.*, vol. 15, pp. 560–563, 2016.

[11] A. Clemente, L. Dussopt, R. Sauleau, P. Potier, and P. Pouliguen, "Wideband 400-element electronically reconfigurable transmitarray in X band," *IEEE Trans. Antennas Propag.*, vol. 61, no. 10, pp. 5017–5027, 467 Oct. 2013.

[12] M. Wang, S. Xu, F. Yang, N. Hu, W. Xie, and Z. Chen, "A novel 1-bit reconfigurable transmitarray antenna using a C-shaped probe-fed patch element with broadened bandwidth and enhanced efficiency," *IEEE Access*, vol. 8, pp. 120124–120133, 2020.

doi:10.6342/NTU202302000

[13] F. Wu, J. Wang, K.-M. Luk and W. Hong, “A Wideband Low-Profile Efficiency-Improved Transmitarray Antenna With Over-1-bit Phase-Shifting Elements,” *IEEE Access*, vol. 8, pp. 32163-32169, 2020.

[14] P. Feng, S. Qu and S. Yang, “Octave Bandwidth Transmitarrays With a Flat Gain,” *IEEE Transactions on Antennas and Propagation*, vol. 66, no. 10, pp. 5231-5238, Oct. 2018.

[15] S. Shi, Q. Lu, W. Feng and W. Chen, “Wideband Polarization Rotation Transmitarray Using Arrow-Shaped FSS at W-Band,” *IEEE Transactions on Antennas and Propagation*.

[16] K. Mavrakakis, H. Luyen, J. H. Booske and N. Behdad, “Wideband Transmitarrays Based on Polarization-Rotating Miniaturized-Element Frequency Selective Surfaces,” *IEEE Transactions on Antennas and Propagation*, vol. 68, no. 3, pp. 2128-2137, Mar. 2020.

[17] H. Yu, J. Su, Z. Li and F. Yang, "A Novel Wideband and High-Efficiency Electronically Scanning Transmitarray Using Transmission Metasurface Polarizer," in *IEEE Transactions on Antennas and Propagation*, vol. 70, no. 4, pp. 3088-3093, April 2022.

[18] C.-W. Luo, G. Zhao, Y.-C. Jiao, G.-T. Chen and Y.-D. Yan, "Wideband 1 bit Reconfigurable Transmitarray Antenna Based on Polarization Rotation Element," in *IEEE Antennas and Wireless Propagation Letters*, vol. 20, no. 5, pp. 798-802, May 2021.

[19] M. T. Nguyen, T. T. Nguyen and B. D. Nguyen, “Wideband Transmitarray Unit-Cell Design With 1-Bit Phase Control and Twistable Polarization,” in *IEEE Microwave and Wireless Components Letters*, vol. 32, no. 6, pp. 627-630, June 2022.

[20] B.-T. Lin and S.-Y. Chen, “Reconfigurable Wideband PIN-Diode-Loaded 1-Bit Unit Cell for Beam-Steering Transmitarray.” 2022 IEEE CAMA, Dec. 2022.

[21] Z. Wei, Y. Cao, Y. Fan, X. Yu, and H. Li, “Broadband polarization transformation via enhanced asymmetric transmission through arrays of twisted complementary split-ring resonators,” *Appl. Phys. Lett.*, vol. 99, no. 22, Nov. 2011, Art. no. 221907.

[22] [Online]. Available: https://www.mouser.tw/datasheet/2/249/MA4AGP907__MA4AGFCP910-1922050.pdf

[23] [Online]. Available: https://docs.macetech.com/doku.php/centipede_shield

[24] [Online]. Available: https://www.ainfoinc.cn/amfilerating/file/download/file_id/1485/

doi:10.6342/NTU202302000